

Steam Torch Plasma Modelling

Jiří Jeništa¹

Received: 1 November 2016 / Accepted: 23 January 2017 / Published online: 2 February 2017
© Springer Science+Business Media New York 2017

Abstract Numerical modelling of physical properties and processes in an electric arc stabilized by a water vortex (steam torch) has been summarized in this review paper. One-fluid MHD equations are numerically solved for an axisymmetric thermal plasma flow inside a discharge chamber of the steam plasma torch. The steady state solution results are discussed for the range of currents 300–600 A with relatively low steam flow rate of about 0.3 g s^{-1} . The maximum obtained velocities and temperatures— 8500 m s^{-1} , 26,300 K, are reported at the centre of the nozzle exit for 600 A. The evaporation of water, i.e. mass flow rate of steam, was predicted from a comparison between the present simulation and experiments. The generated plasma is mildly compressible ($M < 0.7$) with the inertial forces overwhelming the magnetic, viscous, centrifugal and Coriolis forces with the factor of 10^3 . Our calculations showed that the most significant processes determining properties of the arc are the balance of the Joule heat with radiation and radial conduction losses from the arc. Rotation of plasma column due to the tangential velocity component has a negligible effect on the overall arc performance, however, the rotation of water induces fluctuations in the arc and in the plasma jet with characteristic frequency which is related to the frequency of rotation of water. Reabsorption of radiation occurs at the radial position higher than 2.5 mm from the arc axis. The amount of reabsorbed radiation is between 17 and 28%. LTE conditions are satisfied in the arc column with the 2 mm radius. Comparison between the present simulations and experiments shows good agreement with the current–voltage characteristics, radial velocity and temperature profiles, as well as with the other related numerical simulation.

Keywords Arc · Evaporation · Mass flow rate · Water-vortex stabilization · Net emission coefficients · Partial characteristics · Local thermodynamic equilibrium

✉ Jiří Jeništa
jenista@ipp.cas.cz

¹ Institute of Plasma Physics AS CR, v.v.i., Za Slovankou 1782/3, 182 00 Praha 8, Czech Republic

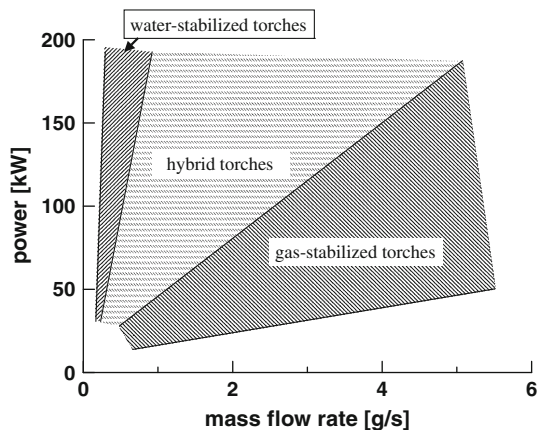
Introduction

Plasma jets generated in dc arc plasma torches operating at atmospheric pressure have been widely used for material processing, plasma cutting, arc welding, decomposition of persistent chemical substances, or waste treatment. Performance characteristics of a torch in specific plasma processing application are determined by plasma jet characteristics, especially by temperature and velocity profiles, by composition of plasma as well as by plasma flow structure and stability. These characteristics can be adjusted for given application by torch design, choice of plasma gas and by arc current. There are some limits of range of adjustable plasma jet characteristics that are given by a principle of stabilization of arc. In commonly used *gas-stabilized plasma torches* the arc is stabilized by flowing gas that flows along the arc column in the arc chamber. Plasma jets with substantially different characteristics can be generated in arcs stabilized by liquid. *Water-stabilized torches (steam torches)* are characterized by very low mass flow rates and high power. Plasma enthalpy is thus several times higher than enthalpy of plasmas generated in gas-stabilized torches. High enthalpy is accompanied by very low plasma density. Other plasma parameters substantially differ from the ones in gas torches as well. A combination of a liquid and gas stabilizations is utilized in *hybrid torches* for better control of plasma characteristics. The hybrid stabilization offers possibility of adjustment of plasma parameters from high enthalpy, low density plasmas typical for liquid stabilized torches to lower enthalpy, higher density plasmas generated in gas stabilized torches. By combination of parameters of the two sections a wide range of plasma characteristics can be obtained. Operation regimes of the three principles are shown in Fig. 1 where a relation between arc power and mass flow rate of plasma is given.

The electric arc with the *stabilization of arc by a water vortex* represents a special type of a transferred plasma torch producing oxygen–hydrogen plasma with extremely high enthalpies. High thermal loading of this arc is possible due to stabilization by wall evaporation. Higher input powers and lower mass flow rates are obtained with respect to wall stabilized and free burning arcs.

The history of water vortex stabilization goes back to the works of Gerdien and Lotz in 1920s [1, 2]. Basic experimental investigations of the water-stabilized arcs were performed in the 1950s by Maecker [3, 4] who studied the effect of the length and diameter of the stabilizing channel. Several experimental studies measured arc plasma temperatures using

Fig. 1 Operation regimes of water-stabilized, gas-stabilized and hybrid plasma torches (courtesy of Dr. Hrabovský)



methods of emission spectroscopy [5–7]. Axial temperatures as high as 50,000 K were presented in these papers.

Water-vortex stabilized electric arc (see Fig. 2) has been intensively studied from the beginning of 1990s to mid 2000s at the Institute of Plasma Physics (IPP) of the Czech Academy of Sciences in Prague. Published experimental paper [8] reports extremely high plasma temperatures ($\sim 30,000$ K) and velocities (~ 7000 m s $^{-1}$). Plasma temperatures for different currents were obtained by the series of spectroscopic measurements [9, 10] and velocities by electric probe diagnostics [11]. The radial transport of energy by radiation was identified as a decisive process controlling arc and plasma parameters. Experimental analysis of the radial energy balance showed that the input power is distributed in the discharge as follows: about 57–87% is transferred in the radial direction, 20–50% is absorbed in water vapours, $\sim 1\%$ is spent for evaporation, and $\sim 40\%$ represents power losses to the water [8].

A principle drawing of the experimental arc chamber is shown in Fig. 3. The chamber is divided into several sections by the baffles with central holes. Water is injected tangentially into the sections and creates the vortex in the chamber. The inner diameter of the vortex is determined by the diameter of the holes in the baffles. Water is exhausted at two positions along the arc chamber. The cathode is made of a carbon rod. The anode made of copper disc with internal water cooling is located outside the arc chamber downstream of the exit nozzle. The anode disc rotates with high circumferential velocity (3000 revolutions per minute) to reduce strong electrode erosion in the surrounding atmosphere containing oxygen. The length of the part of the arc column stabilized by water vortex inside the arc chamber is 60 mm, the inner diameter of the vortex is 7 mm, the diameter of the exit nozzle is 6 mm and its length is 5 mm. The length of the part of arc column outside the chamber between the exit nozzle and the anode is varying between 3 and 15 mm as the anode attachment moves along the anode surface.

Water is injected into the chamber under pressures of 0.39 MPa (0.6 MPa) with flow rates of 10 l min $^{-1}$ (16 l min $^{-1}$). Higher pressures insure better hydrodynamic stability of the arc. The stabilizing wall is formed by the inner surface of water vortex created in the arc chamber. Evaporation of water is induced by the absorption of a fraction of Joule power dissipated within the conducting arc core. Further heating and ionization of the steam are the principal processes which produce water plasma. The continuous inflow and heating lead to an overpressure and plasma is accelerated towards the nozzle exit. The arc properties are thus controlled by the radial energy transport from the arc core to the walls

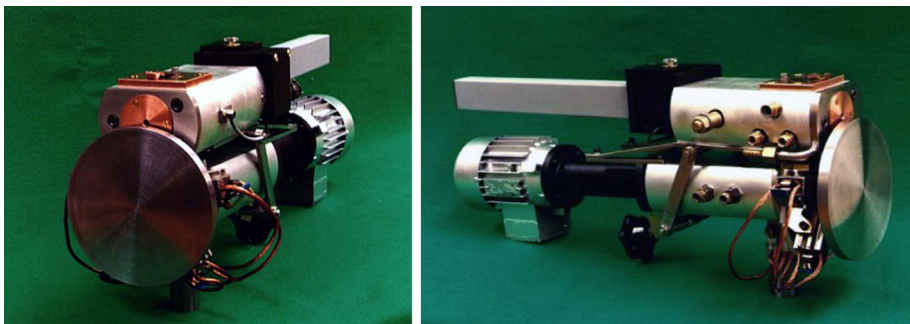


Fig. 2 Water-vortex stabilized plasma torch. The main parts are the discharge chamber, the water-cooled anode rotating disc, and the consumable graphite cathode

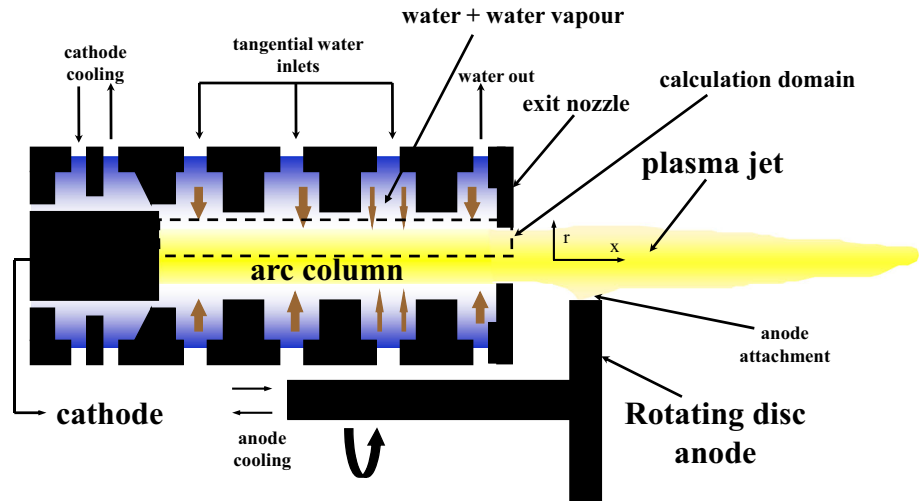


Fig. 3 Principle drawing of the experimental arc chamber

and by the processes influencing evaporation of the liquid wall. Radiation from the arc is the principal process responsible for power balance. Part of the radiation is transferred in the axial direction of the plasma jet, the other part in the radial direction is partially reabsorbed in water vapours and the rest of radiation is absorbed in the water vortex, heating such water that is exhausted from the chamber. Radiation damage of the chamber walls is negligible.

The water plasma torch exhibits special performance characteristics; i.e. high outlet velocities, temperatures, plasma enthalpy and, namely, high powder throughput, compared to commonly used gas-stabilized torches [12]. This kind of arc was successfully designed in 1960s for plasma cutting [13]. The main research application of the water torch at IPP is plasma spraying of metallic or ceramic powders (TiO_2 , Al_2O_3 , ZrSiO_4 , W-based, Ni-based alloys, Al, steel) injected into the plasma jet. Some of the studies of physical and chemical processes in materials after their interaction with plasma can be found, e.g., in [14–17]. Recently, an experimental plasmachemical reactor PLASGAS equipped with the spraying torch WSP[®]H (the hybrid stabilized torch) has been employed for the innovative and environmentally friendly plasma treatment of waste streams with a view to their sustainable energetic and chemical valorization and to a reduction of the emission of greenhouse gases [18–20]. Pyrolysis of biomass was experimentally studied in the reactor using crushed wood and sunflower seeds as model substances. A high content of combustible mixture of hydrogen and carbon monoxide was produced (syngas).

Steam is also used as the plasma-producing gas in the Westinghouse torch and in the torch developed by the Chemistry Laboratory of Plasmas at the University Limoges [21]. In the French torch, a small flow of a non-oxidizing gas such as argon protects the cathode against corrosion.

A number of the original papers concerning the modelling of the water-vortex stabilized arc at IPP was published by Jeništa. In [22] the basic physical properties and processes are discussed from the results of 2D axisymmetric model. The computer results were carried out for the current range 300–600 A. Velocities up to 7 km s^{-1} and temperatures up to 22 kK were reported. Forces acting in the discharge were discussed from the similarity

fluid dynamic and magnetohydrodynamic numbers. It was shown that the tangential motion of the arc has a negligible effect on the torch performance and energy balance. The influence of non-uniform evaporation rate of steam along the effective water-vapour-boundary on the outlet torch parameters was studied in [23]. Radiation is here calculated using the net emission coefficient method as in the previous paper [22] but the radiation flux near the water-vapour-boundary is estimated by the method of radiation view factors. The influence of virtual anode position on arc parameters were studied by Gonzalez and Jeništa [24]. An iterative procedure to determine the radius of the effective water-vapour-boundary was proposed in [25]. Based on a comparison with experiments, the most probable radius was set up to 3.3 mm. Evaporation mass flow rates of steam were specified in the iterative procedure. The validity of local thermodynamic equilibrium conditions within the arc were also studied [25, 26]. Radiation from the arc using the partial characteristics method and a comparison of the results with the net emission coefficient method was presented in [27, 28]. It was shown that reabsorption of radiation occurs in arc fringes with the radial positions higher than 2.5 mm from the arc axis. Reabsorption in the amount of 25–29% was reported. Comparison of performance between the water- and hybrid-stabilized arcs is presented in [29, 30]. The contribution of O_2 , H_2 and OH molecular bands to the amount of reabsorbed radiation was also discussed.

Modelling of two-phase system water-vapour in a real experimental geometry has been also attempted using the commercial computational fluid dynamic code Fluent [31]. The profile of the phase transition water-steam was obtained by employing an artificial heat source inside the chamber (not a real plasma).

Two-dimensional axisymmetric model based on the finite elements method for the description of plasma not only inside but also outside the discharge chamber was developed by Kotalík [32–35]. This model enabled to calculate temperature and flow fields in the discharge and in the plasma jet, electrical characteristics, interaction of plasma with powder particles injected into the plasma jet and the nozzle shape optimization regarding the outlet plasma temperature and velocity. For arc currents 300–600 A, the respective temperatures and velocities in the range 16,700–26,400 K and 2300–6900 $m\ s^{-1}$ are obtained at the centre of the nozzle exit corresponding well with the experimental values. Despite some differences in the boundary conditions in Kotalík's and Jeništa's models, both models provide comparable results for the most of the calculated physical quantities. Some other works of Kotalík are related to interaction of a sprayed particle with surrounding plasma (Stefan problem), i.e. the solution of the heat transfer equation with phase transition [36, 37] describing the interaction between plasma and powder particles.

Some other papers related to modelling of direct-current (non)transferred-arc steam torch at atmospheric pressure were published by Chau [38–40]. Since his plasma torch has the geometry of a hollow pipe, the studied plasma flow with transferred arc can be treated as an axisymmetric problem. The arcs in this configuration operate at high currents (180–900 A) with a strong vortex flow structure. For non-transferred torch the predicted result suggests that the steam plasma can be accelerated to a mean velocity of 1500 ms^{-1} at torch outlet with the mass flow rate of 5 gs^{-1} and the system current of 180 A. Nonequilibrium model of steam plasma in a nontransferred direct-current torch was published in [40].

The present paper reports the principal numerical results obtained by the author on the water-vortex stabilized arc (steam plasma torch) during the years 1997–2006. Nevertheless, it should be point out that the present review is not just only a collection of the results in my old papers. Some results are published here either for the first time or in a new form. “Physical model” section gives information about the model assumptions, physical model,

boundary conditions and numerical scheme. “Results of Calculation” section, divided into five subsections, reveals the most important findings.

Physical Model

Assumptions and the Set of Equations

The following assumptions are applied:

1. the model is two-and-half dimensional with the discharge axis as the axis of symmetry,
2. the plasma flow is laminar and compressible,
3. the water plasma itself is in local thermodynamic equilibrium,
4. radiation losses are calculated by the net emission coefficients and partial characteristics,
5. gravity effects and viscous dissipation are negligible,
6. the magnetic field is generated only by the arc itself,
7. processes in the cathode potential fall were omitted.

The comments to some of these assumptions are given below. The set of governing equations is written for a computer implementation in an axisymmetric cylindrical system of coordinates. The governing equations read as follows:

continuity equation:

$$\frac{\partial}{\partial t} \rho + \frac{1}{r} \frac{\partial}{\partial r} (\rho vr) + \frac{\partial}{\partial x} (\rho u) = 0, \quad (1)$$

momentum equations:

$$\begin{aligned} \rho \frac{\partial u}{\partial t} + \rho v \frac{\partial u}{\partial r} + \rho u \frac{\partial u}{\partial x} = & -\frac{\partial p}{\partial x} + j_r B_\theta - \frac{2}{3} \frac{\partial}{\partial x} \left[\eta \left(\frac{1}{r} \frac{\partial}{\partial r} (rv) + \frac{\partial u}{\partial x} \right) \right] \\ & + \frac{\partial}{\partial x} \left(2\eta \frac{\partial u}{\partial x} \right) + \frac{1}{r} \frac{\partial}{\partial r} \left[r\eta \left(\frac{\partial u}{\partial r} + \frac{\partial v}{\partial x} \right) \right], \end{aligned} \quad (2)$$

$$\begin{aligned} \rho \frac{\partial v}{\partial t} + \rho v \frac{\partial v}{\partial r} + \rho u \frac{\partial v}{\partial x} = & -\frac{\partial p}{\partial r} - j_x B_\theta - \frac{2}{3} \frac{\partial}{\partial r} \left[\eta \left(\frac{1}{r} \frac{\partial}{\partial r} (rv) + \frac{\partial u}{\partial x} \right) \right] + \frac{\rho w^2}{r} \\ & + \frac{1}{r} \frac{\partial}{\partial r} \left(2\eta r \frac{\partial v}{\partial r} \right) - \frac{2\eta v}{r^2} + \frac{\partial}{\partial x} \left[\eta \left(\frac{\partial u}{\partial r} + \frac{\partial v}{\partial x} \right) \right], \end{aligned} \quad (3)$$

$$\rho \frac{\partial w}{\partial t} + \rho v \frac{\partial w}{\partial r} + \rho u \frac{\partial w}{\partial x} = \frac{1}{r} \frac{\partial}{\partial r} \left(\eta r \frac{\partial w}{\partial r} \right) + \frac{\partial}{\partial x} \left(\eta \frac{\partial w}{\partial x} \right) - \frac{\rho vw}{r} - \frac{\eta w}{r^2} - \frac{w}{r} \frac{\partial \eta}{\partial r}, \quad (4)$$

energy equation:

$$\begin{aligned} \rho c_p \frac{\partial T}{\partial t} + \rho v c_p \frac{\partial T}{\partial r} + \rho u c_p \frac{\partial T}{\partial x} - \frac{\partial p}{\partial t} = & u \frac{\partial p}{\partial x} + v \frac{\partial p}{\partial r} + j_r E_r + j_x E_x \\ & + \frac{1}{r} \frac{\partial}{\partial r} \left(r\lambda \frac{\partial T}{\partial r} \right) + \frac{\partial}{\partial x} \left(\lambda \frac{\partial T}{\partial x} \right) + \frac{5k}{2e} \left(j_x \frac{\partial T}{\partial x} + j_r \frac{\partial T}{\partial r} \right) - U_{net}, \end{aligned} \quad (5)$$

charge continuity equation:

$$\frac{1}{r} \frac{\partial}{\partial r} \left(r\sigma \frac{\partial \Phi}{\partial r} \right) + \frac{\partial}{\partial x} \left(\sigma \frac{\partial \Phi}{\partial x} \right) = 0, \tag{6}$$

where x and r are the axial and radial coordinates, u , v and w are the axial, radial and tangential components of the velocity respectively, ρ is the mass density, p is the pressure, T is the temperature, j_x and j_r are the axial and radial components of the current density, E_x and E_r are the axial and radial components of the electric field strength, Φ is the electrical potential, k is the Boltzmann constant and e is the elementary charge of the electron. The transport properties of atmospheric pressure water plasma (where λ is the thermal conductivity, σ is the electrical conductivity, η —the dynamical viscosity) as well as the thermodynamic properties (where ρ is the mass density and c_p is the specific heat under constant pressure) implemented in this model were calculated rigorously from the kinetic theory [41].

Compressible effects in the momentum equations are presented by the terms

$$-\frac{2}{3} \frac{\partial}{\partial x} (\eta \cdot \text{div} \vec{u}), \quad -\frac{2}{3} \frac{\partial}{\partial r} (\eta \cdot \text{div} \vec{u});$$

and in the energy equation by the compression work terms $\vec{u} \cdot \nabla p$. Nevertheless, in the expected range of the Mach numbers 0.3–0.7, the absolute magnitude of the compressible terms with respect to the other terms in Eqs. (1–5) is supposed to be small. The electron enthalpy heating term

$$\frac{5k}{2e} \vec{j} \cdot \nabla T$$

in the energy equation could contribute substantially near the cathode region but since the cathode layer is not included in the model this term is expected to be small.

A few comments should be mentioned on the assumptions of the model:

1. The assumption 1) means that the tangential component of velocity w is independent of the tangential coordinate θ so that the distribution of the tangential velocity is the same for all θ angles. The only effect of the tangential velocity on the plasma flow is through the centrifugal force $\rho w^2/r$ in the radial velocity equation. A justification of the axisymmetric assumption comes out from these considerations:

The cylindrical discharge chamber (Fig. 3) is divided into several sections by the baffles with central holes. Water is injected tangentially into the chamber by three sets of three inlet holes (totally 9 holes) placed equidistantly along the circumference at angles of 120°. The inner diameter of the water vortex is determined by the diameter of the holes in the baffles. Water is usually pumped under pressures of 0.39 MPa (0.6 MPa) with flow rates of 10 l min⁻¹ (16 l min⁻¹). Higher pressures insure better hydrodynamic stability of the arc. Since water flows in a closed circuit, it is also exhausted at two positions along the arc chamber.

In experiment, the distance from the exit nozzle to the anode can be changed from 5 to 20 mm. It can be expected that regions close to the exit nozzle will remain undisturbed by the presence of the anode, while the more distant regions (15–20 mm) will be influenced by 3D effects (the anode jet and anode processes). A validity of the axisymmetric assumption is due to a) cylindrical symmetry of the discharge chamber setup, b) tangential injection of water through the holes along the circumference, and c) the flexible distance between the nozzle exit and anode.

2. The assumption of laminar flow is based on experiments, showing the laminar structure of the plasma flowing out of the discharge chamber in the space between the nozzle exit and the anode. The laminar flow has been observed for currents up to 600 A. It comes out from our previous calculation [22] that Reynolds number based on the outlet diameter 6 mm reaches in the axial region 13,000 at maximum and decreases to 300 in arc fringes.
3. LTE conditions in the arc will be discussed in more detail in “Non-equilibrium Effects” section. The fulfilment of LTE conditions can be expected in the hot arc core due to high currents.
4. The electric potential drops between the cathode and the outlet nozzle are up to 210 V. The cathode fall with the drops of several volts cannot influence substantially the overall results.

Radiation losses from the water arc plasma are included through the net emission coefficient U_{net} which is a function of local temperature with optical thickness corresponding to the discharge radius (~ 3.3 mm). This model has been applied, for example, in [22]. The net emission coefficient model provides very good approximation for isothermal plasmas with included self absorption of radiation in hot plasma regions, but not in colder arc fringes.

The net emission coefficient is composed of three components: the continuum, the resonance lines which are partially self-absorbed within the plasma and the other lines which are not absorbed [42]. For the optical thickness 3–4 mm considered in this modelling, the emission coefficient of water is very close to that of pure oxygen due to the strong absorption of the hydrogen Lyman lines. The radiation comes out mainly from the bremsstrahlung continuum, few lines of OI (e.g. 777.34, 793.93 nm), several tens of OII lines with wavelengths ranging between 395 and 495 nm, and H_{β} line of Balmer series (486.113 nm) [43].

Another radiation model including some basic results was applied in “Reabsorption of Radiation in the Arc” section.

Boundary Conditions and Numerical Scheme

The calculation region and the corresponding boundary conditions are presented in Fig. 4 (see also a position of the calculation domain in Fig. 3). The dimensions are respectively

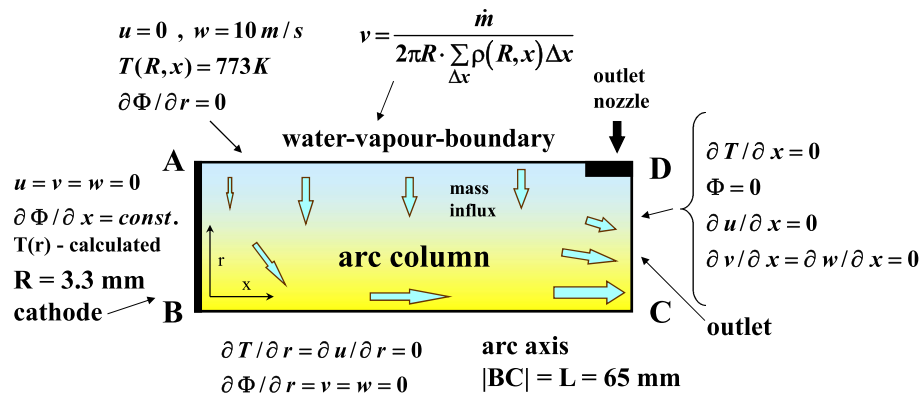


Fig. 4 Discharge area geometry and boundary conditions

$R = 3.3$ mm and $L = 65$ mm for the radius and the length. Here u , v and w are the axial, radial and tangential components of velocity.

- (a) *Cathode surface* (AB) Along the cathode surface AB we assume no slip conditions for velocities, i.e. $u = v = w = 0$ m s⁻¹. Because of the lack of experimental data, we prescribed different forms of temperature profiles (polynomial, Gaussian). Numerical tests (unpublished) showed a weak dependence of the form of the temperature profile on the overall solution. Thus we decided to calculate the temperature profile and the electric field strength iteratively from the Elenbaas–Heller equation with the radiation term (a model approach for electric arc in the immobile gas), before the fluid-dynamic calculation itself, to obtain the prescribed current level and the electric field strength near the cathode surface.
- (b) *Axis of symmetry* (BC) The zero radial and tangential velocities and symmetry conditions are specified here.
- (c) *Arc gas outlet plane* (CD) The outlet velocity profile is determined approximately from the condition of conservation of the total mass flow. The zero electric potential (the reference value) and zero axial derivatives of temperature, radial and tangential velocities are also defined at CD.
- (d) *Water-vapour-boundary and outlet nozzle* (DA) Along this line we specify the so-called “effective water vapour boundary” with a prescribed temperature of water vapour 773 K (explained in more detail in “[Determination of Evaporation Mass Flow Rate and The Radius of the Discharge Region](#)” section). This is our numerical simplification of the more complex physical reality assumed near the phase transition water-vapour in the discharge chamber, like interaction between water vortex and vapour, time-dependent form, or splitting of the phase transition, etc. The same temperature 773 K is ascribed to the outlet nozzle with the dimensions 5 and 0.3 mm in the axial and radial directions. (Of course, the nozzle temperature can change depending on arc current and need not be uniform within the nozzle volume. Such assumption can be found in [22]). Because of zero current density in cold vapour region (no current goes outside through the lateral domain edges), $E_r = 0$ V m⁻¹ at DA. The magnitude of the radial inflow velocity is assumed to be uniform along the axial direction and it is calculated from a given evaporation steam flow rate (details are in “[Determination of Evaporation Mass Flow Rate and The Radius of the Discharge Region](#)” section). The axial velocity of water vapour at DA is zero and the magnitude of the tangential velocity is estimated from simplified analytical expressions by Maecker [3] and it is put 10 m s⁻¹ (discussed in “[Effect of the Tangential Velocity Component on the Arc Discharge Performance](#)” section).

The solution of the Eqs. (1–6) was carried out using a compressible version of the control volume method based on the iteration procedure SIMPLER [44], developed by the author, which uses both the main and staggered grid lines. Pressure–density corrections were employed in the pressure and pressure-correction equations in the original incompressible SIMPLER code to deal with a compressible flow properly. Since the iteration procedure is pressure-based, density as a function of temperature and pressure must be known in advance (from the equation of state of ideal gas, [41]). The power-law scheme of the 5th order in the convection–diffusion term is employed. The set of discretized algebraic equations is solved by a line-by-line method, i.e. the combination of the Gauss–Seidel method and the tri-diagonal matrix algorithm (TDMA) for speeding up the convergence. Pressure, velocities, temperature and electric potential are calculated from (1 to 6). The code is written in the Fortran language. The final steady state was reached as a result of a

time evolution of the initial state. A grid-independence study was carried out for several grids (for example, for 31×31 , 61×21 , 121×61 , 216×61 grid points in the axial and radial directions respectively) up to the finest grid with 500×81 grid points. Considering the computer time and the number of computer runs for different input parameters, I have finally chosen for the present calculations a non-equidistant orthogonal main grid with 61×41 points for the axial and radial directions respectively. Numerical tests confirmed that the relative difference of calculated physical quantities for grids with 61×41 and 500×81 points, taken either as a value (electric potential, overpressure), or averaged through the radial coordinate at the outlet nozzle exit (temperature, velocity), are a few per cent: 1.2% for the electric potential, 1.2% for the temperature, 6.1% for the velocity, 8.6% for the overpressure.

Results of Calculation

Determination of Evaporation Mass Flow Rate and the Radius of the Discharge Region

Production of steam by evaporation of a small part of water vortex, i.e. evaporation mass flow rate \dot{m} , is very important physical parameter determining all the basic properties of the vortex-stabilized arc. Its value is defined by energy balance of the arc itself for given operating conditions and cannot be changed by user. Since the discharge operates deeply inside the discharge chamber equipment and is not accessible by any diagnostics, evaporation mass flow rate cannot be measured directly in experiments. One way to determine \dot{m} approximately from the integral energy balance is as follows: let us neglect, in the energy Eq. (5), the terms corresponding to compression work, axial conduction and electron enthalpy and let us assume that the radial velocity is much smaller than the axial one. Integrating such a simplified steady-state energy equation over the discharge volume provides the equation

$$\int_0^R 2\pi r \rho u h dr = L(I \cdot E - Q_w - \dot{m} Q_{ev}), \quad (7)$$

where h is the enthalpy of plasma, Q_w is the radiated power absorbed in water and/or in the walls of the stabilizing chamber, Q_{ev} is the energy per unit mass spent for heating of water to the boiling temperature and for the phase change, and L is the discharge length. Assuming that the Mach number M is independent of radius, the formula for calculating M takes the form

$$M = \frac{L(I \cdot E - Q_w)}{\int_0^R 2\pi \rho c h r dr + [l_v + c_w(T_w - T_0)] \int_0^R 2\pi \rho c r dr}, \quad (8)$$

where c is the velocity of sound and l_v is the specific heat of evaporation for water. By measuring I , $E \cdot L$, Q_w and $T(r)$, and knowing the temperature dependencies $\rho(T)$, $c(T)$ and $h(T)$, we are able to determine M and \dot{m} . Such an approximate approach was chosen in [8] with finding the values of \dot{m} for the current range 300–600 A; namely, $\dot{m} = 0.204 \text{ g s}^{-1}$ (300 A); 0.272 g s^{-1} (400 A); 0.285 g s^{-1} (500 A) and 0.325 g s^{-1} (600 A).

In my first simulations I used these experimentally determined values of \dot{m} to see the agreement or disagreement with experiments. The result is summarized in Table 1 which compares the numerical results (at the point C of the computational domain) with the experimental ones (measured 2 mm downstream from the nozzle [45]). The characteristics presented in Table 1 are the axial velocity, temperature, potential drop between the cathode and the nozzle (point C), pressure drop between the cathode and the nozzle, current density and electric field strength. The input power means the product of current and the potential drop; the term total losses stands for the power losses due to radial conduction and radiation, these losses are also shown in the last item as a per cent of the input power.

We can see that typical outlet velocities are 2.5–7 km s⁻¹, temperatures 19,000–27,000 K, the voltage drop ~200 V and the pressure drop 0.06–0.25 atm. The magnitudes of all presented characteristics increase with current as can be expected for increasing powers to the arc and evaporation mass flow rates. Despite the axial velocities are very high, the Mach numbers at the point C range from 0.3 to 0.7 because of the temperature-dependent speed of sound. The plasma flow is thus mildly compressible. A satisfactory correspondence between the numerical and experimental data, if available, is obvious. The higher differences occur in temperature, namely for higher currents. The lower numerical values can be caused, in my opinion, by the fact that we neglected absorption of radiation in colder arc regions and water vapour and by the properties of the chosen net emission coefficients radiation model. A more complicated shape of the water–water-vapour (water-steam) phase transition than that approximated by the direct line AD can also be of significant importance. The input power $I \cdot \Phi$ increased more than twice for the 600 A arc with respect to the 300 A value. The power losses from the arc are the sum

Table 1 Comparison between experimental and numerical values of the axial quantities for currents 300–600 A and for evaporation mass flow rates determined from experimental measurements

Parameters	$I = 300$ A, flow rate = 0.204 g s ⁻¹		$I = 100$ A, flow rate = 0.272 g s ⁻¹		$I = 500$ A, flow rate = 0.285 g s ⁻¹		$I = 600$ A, flow rate = 0.325 g s ⁻¹	
	Exp.	Num.	Exp.	Num.	Exp.	Num.	Exp.	Num.
u (m s ⁻¹)	2494	2080	4407	3840	5649	4590	7054	6950
T (K)	19,000	17,200	23,000	20,400	26,200	18,900	27,200	21,900
Φ (V)	185	182	190	203	200	191	216	206
Δp (Pa)	6100	7220	12,800	13,000	16,700	21,000	25,700	30,000
J (current density) (A m ⁻²)	n/a	3.00×10^7	n/a	3.42×10^7	n/a	3.80×10^7	n/a	4.08×10^7
E (electric field strength) (V m ⁻¹)	n/a	3340	n/a	3570	n/a	3940	n/a	4340
Power (W)	n/a	54,800	n/a	81,100	n/a	95,600	n/a	123,300
Total losses (W)	n/a	25,300	n/a	37,000	n/a	54,000	n/a	65,500
Total losses (%)	n/a	46.20	n/a	45.70	n/a	56.50	n/a	53.10

of the radial conduction power and radiation power leaving the discharge which are considered as the two principal processes responsible for power losses. They change slowly with current and represent around 50% of the input power. The rest of the input power is, according to this model, spent for convection, heating and ionization of the plasma.

The next steps to make the \dot{m} values more accurate were presented in [22] where the most probable values of \dot{m} were found by comparing differences between numerical and experimental quantities at the nozzle outlet (axial temperature and velocity) and by comparing the electric potential drop in the chamber. It was found that the best-fit values of $\dot{m} = 0.250 \text{ g s}^{-1}$ (300 A); 0.317 g s^{-1} (400 A); 0.342 g s^{-1} (500 A) and 0.330 g s^{-1} (600 A) correspond to the minimum differences. These values are by about 20% higher than the experimental \dot{m} values.

The results of a new comparison are summarized in Table 2. In contrast to Table 1, axial velocities, pressure drops, Mach numbers and electric potentials are closer to the experimental values. Temperatures remain practically unchanged. On the other hand, electrical characteristics (current density, electric field strength) and the total losses slightly decreased.

The last and more detailed determination of \dot{m} was presented in [25]. Here the values of \dot{m} were changed simultaneously with the radial position of the water-vapour-boundary to meet the condition of minimum differences between experiments and simulations (again—the outlet axial temperature, velocity and the electric potential drop were chosen for a comparison), assuming the fixed temperature of steam at the water-vapour-boundary. Two kinds of radiation model were taken into account—the net emission coefficients method with [46] and without [22] reabsorption of radiation. Some of the physical quantities were

Table 2 Comparison between experimental and numerical values of the axial quantities for currents 300 – 600 A with the numerically best-fit evaporation mass flow rates

Parameters	$I = 300 \text{ A}$		$I = 400 \text{ A}$		$I = 500 \text{ A}$		$I = 600 \text{ A}$	
	Exp.	Num.	Exp.	Num.	Exp	Num.	Exp.	Num.
\dot{m} (g s^{-1})	0.204	0.250	0.275	0.317	0.285	0.342	0.325	0.330
u (m s^{-1})	2494	2490	4407	4400	5649	5660	7054	7050
T (K)	19,000	16,700	23,000	20,400	26,200	19,700	27,200	21,900
Φ (V)	185	185	190	204	200	197	216	206
Δp (Pa)	6100	10,000	12,800	16,800	16,700	28,300	25,700	31,300
M	0.317	0.362	0.445	0.518	0.505	0.705	0.617	0.756
J (current density) (A m^{-2})	n/a	2.76×10^7	n/a	3.43×10^7	n/a	3.79×10^7	n/a	4.07×10^7
E (electric field strength) (V m^{-1})	n/a	3160	n/a	3580	n/a	3910	n/a	4330
Power (W)	n/a	55,500	n/a	81,700	n/a	98,700	n/a	123,700
Total losses (W)	n/a	24,300	n/a	35,700	n/a	50,800	n/a	65,100
Total losses (%)	n/a	43.80	n/a	43.70	n/a	51.40	n/a	52.60

better approximated when using one radiation model, and the others using the second radiation model. Finally, the radius of the water-vapour-boundary was found to be 3.31 mm, similarly as in my previous simulations (3.3 mm). The final corresponding values of \dot{m} are: 0.228 g s⁻¹ (300 A); 0.315 g s⁻¹ (400 A); 0.329 g s⁻¹ (500 A) and 0.363 g s⁻¹ (600 A). The results shown in the next Sections were calculated using these mass flow rates and 3.3 mm as the water-vapour-boundary radius.

Basic Results: Arc Properties and Physical Processes in the Discharge

To see the overall picture of some quantities, we present two-dimensional (2D) contour plots. Figures 5 and 6 comprise contours of the axial velocity, stream function, pressure, Mach number, magnetic induction and the electric potential for the 300 A discharge [the axial position 0 mm (65 mm) corresponds to the cathode (outlet)]. The axial velocity increases with axial distance because of continuous inflow of cold vapour; the maximum velocity 2558 m s⁻¹ occurs at the outlet. Since the density of plasma decreases with temperature, the majority of the discharge mass is carried away in the last millimetre of the discharge radius (see the stream function, the radial distribution at the orifice). The radial

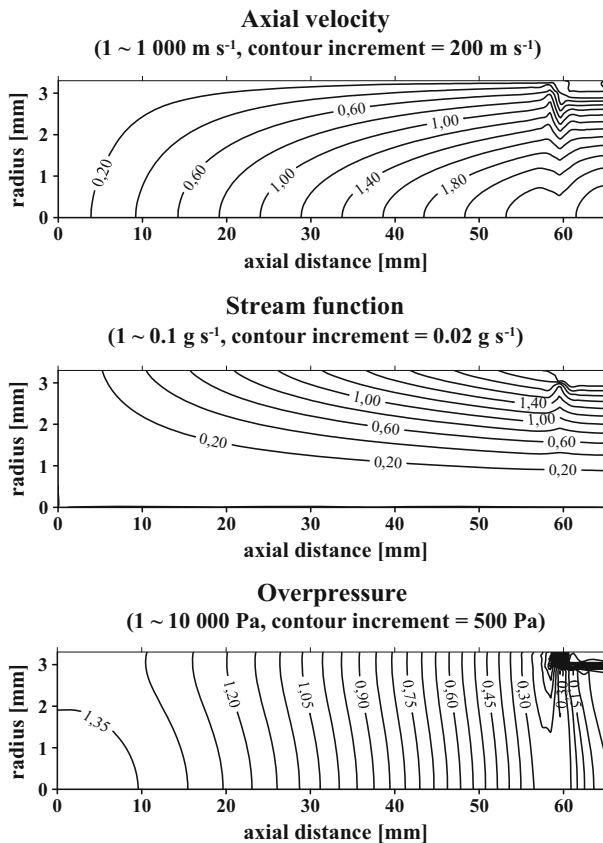


Fig. 5 Contours of fluid-dynamic quantities. Current $I = 300$ A, mass flow rate = 0.228 g s⁻¹. The left (bottom) axis corresponds to the AB (BC) line in Fig. 4

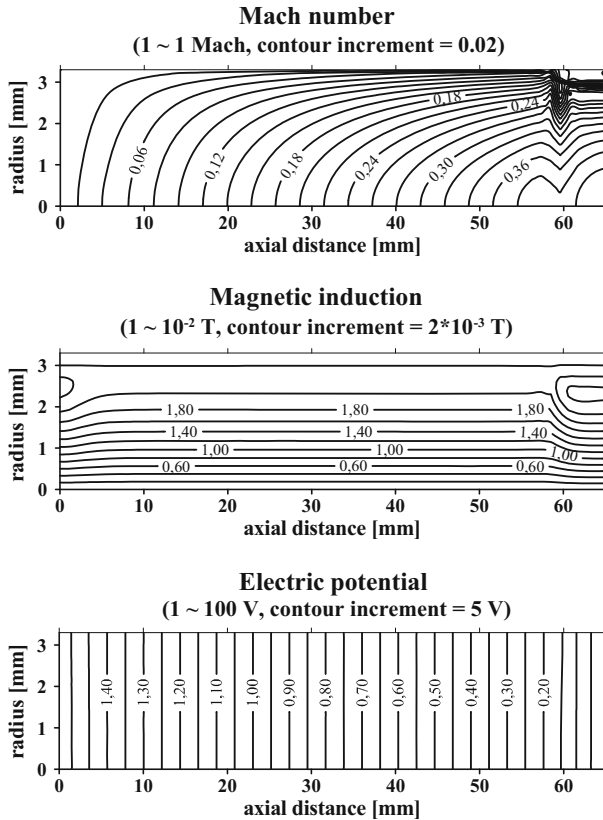


Fig. 6 Contours of the Mach number, magnetic induction and electric potential in the discharge chamber. Current $I = 300$ A, mass flow rate = 0.228 g s⁻¹

component of pressure practically diminishes at the outlet due to the presence of the outlet nozzle. The maximum pressure gradient occurs along the axis (the pressure drop ~ 0.136 atm.). The Mach number is not constant at the exit aperture which means that the prediction of mass flow rate from the measured temperature profiles and from transport and thermodynamic coefficients can experience larger error (the assumption of constant Mach number across the orifice was applied for the determination of mass flow rates from experimental data). The magnetic induction contours, of the order of 10⁻² T, are nearly parallel with the axis within the discharge, except for the cathode and outlet regions. The dominant component of the current density is the axial one which is obvious from the nearly perpendicular contours of the electric potential to the axis.

The temperature contours for 300 and 600 A reveal that there exists an approximately thermal asymptotic region at a distance between 2 and 5 cm from the cathode (Fig. 7). The low-temperature region ($T < 10^4$ K) is wider for the 300 A discharge (~ 1.0 mm), implying a thinner conducting arc core.

Figure 8 (left) demonstrates the influence of the temperature distribution inside the discharge channel on the radial conduction heat flux, depending on the radial temperature gradient and on the value of the strongly temperature-dependent thermal conductivity. The maxima of the conduction heat flux are located in low temperature regions (between 2.6

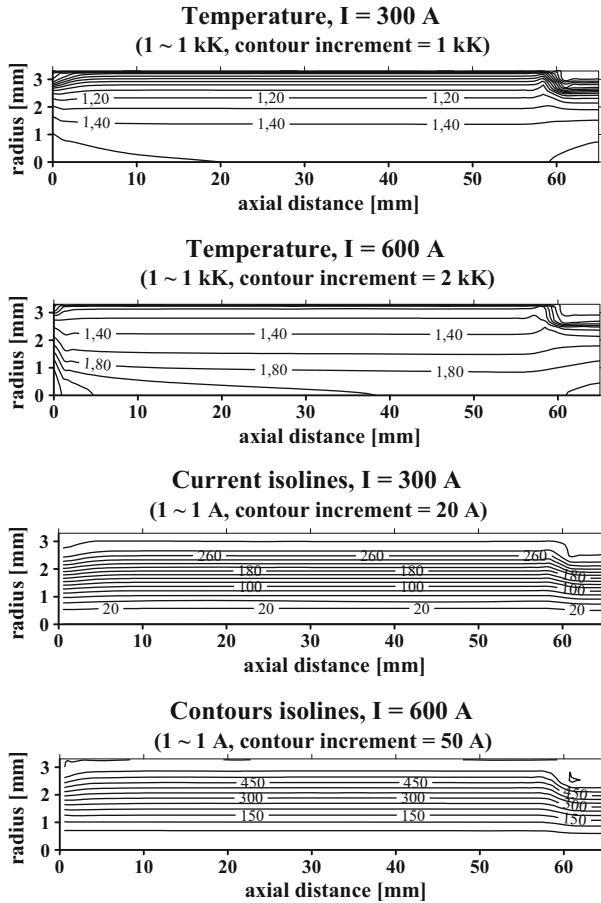


Fig. 7 Contours of the temperature and current flow lines for 300 A (mass flow rate = 0.228 g s⁻¹) and for 600 A (mass flow rate = 0.363 g s⁻¹)

and 3 mm) with steep temperature gradients and the peak value is higher than $2 \times 10^7 \text{ W m}^{-2}$ for 600 A.

The influence of both temperature and velocity fields on the radial convection heat flux $\rho v h$ (h is the enthalpy of plasma) is reflected in Fig. 8 (right). The minus sign is caused by the influx of water vapour into the discharge chamber. The discharge temperature and radial velocity increase with current, thus the convection heat flux is higher for higher currents; for 600 A the peak value of $\sim 1.4 \times 10^8 \text{ W m}^{-2}$ is nearly four times higher than for the 300 A arc. The highest radial convection heat fluxes occur between 1.5 and 2 mm from the arc axis.

It is important to know which physical processes are dominant in the discharge and how they change with current. For this purpose we made absolute magnitudes of all terms in the momentum and energy Eqs. (2-5) within the discharge volume for different currents and we calculated their bulk magnitudes. The so called α parameter equals the ratio of the bulk magnitude of the specific term to the sum of the bulk magnitudes in the momentum (or

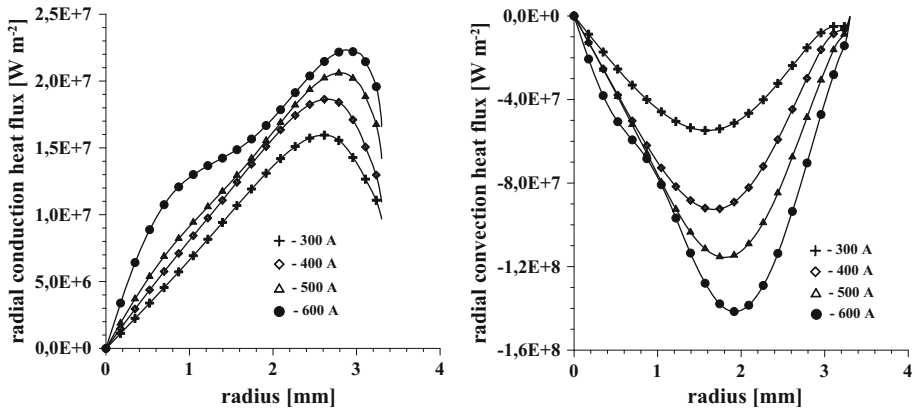


Fig. 8 Radial conduction (*left*) and convection (*right*) heat fluxes at the axial position 4.09 cm from the cathode (the nearly fully-developed temperature region)

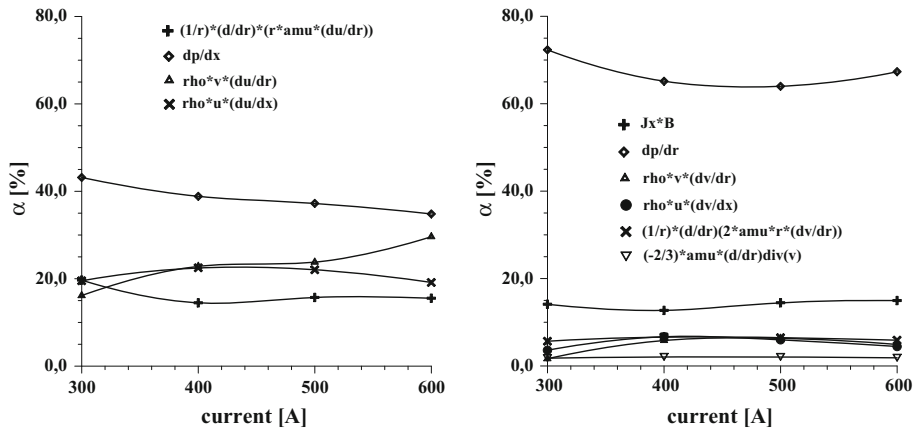


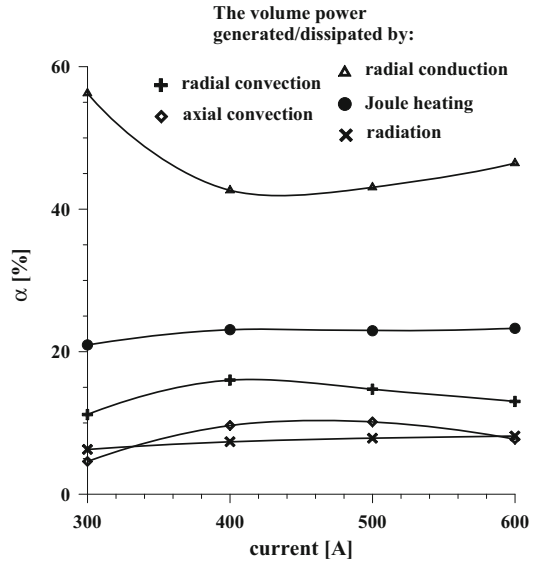
Fig. 9 The bulk magnitudes of the significant terms in the axial momentum (*left*) and radial momentum (*right*) equations with respect to the bulk sum of all terms α (%) as a function of arc current

energy) equation. The results are depicted in Figs. 9 and 10 where the y-axis shows α in per cent's.

The most dominant term in the axial momentum equation is the axial gradient of pressure (Fig. 9). The other terms, like the convection terms and the diffusion of the axial velocity in the radial direction, are comparable in their magnitudes ($\sim 20\%$). The driving forces in the radial momentum equation are the radial pressure gradient, followed by pressure force due to the self-generated magnetic field (Lorentz force). The lower importance, of about 5%, represent convection and diffusion of the radial velocity in the radial direction. The diffusion due to compressible effects (the term with $-2/3$) is the lowest among these terms and represents about 1%.

In the energy equation (Fig. 10), the following processes were recognized as the most significant: radial convection, axial convection, radial conduction, the Joule heating and radiation. Since the conduction acts in the whole region of the discharge and radial temperature gradients are very steep, the bulk value of the energy losses by radial conduction

Fig. 10 The same as in Fig. 9 but for the energy equation. The highest contributions are due to the Joule heat and the power losses by radial conduction



is dominant. The second highest term is the Joule heat, followed by the power transported by radial convection. The smallest two terms, radiation losses from the arc and the power transported by axial convection, which are dominant in central regions of the arc, but occupying a small discharge volume with low density plasma, are of a comparable magnitude, between 5 and 10%.

The dimensionless fluid-dynamic and heat transfer numbers M , Re , Pr , Pe as a function of evaporation mass flow rate for 300 A have been calculated to characterize processes within the arc discharge (Fig. 11). The Reynolds number is based on the diameter of the outlet orifice and all numbers are averaged through the orifice cross section. One can

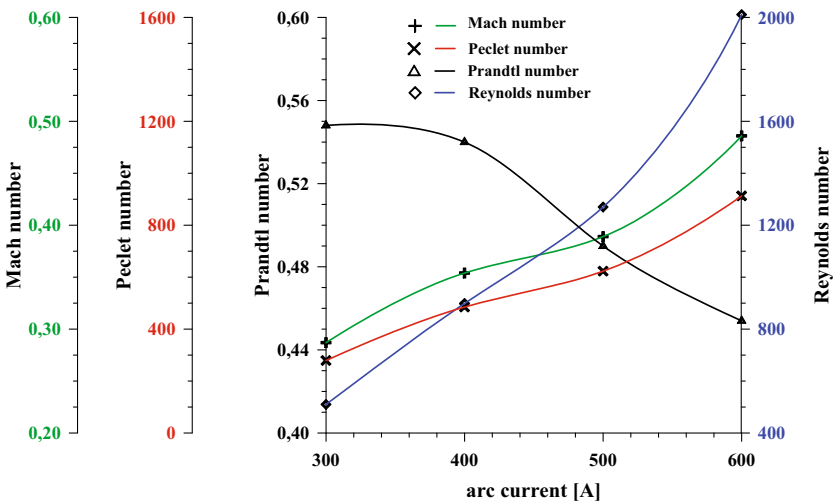


Fig. 11 Dimensionless heat and mass transfer numbers as a function of arc current

observe that for higher current, plasma becomes more compressible and thermal diffusion as well as the role of convection increases (the Peclet number increases). The viscous stresses are more significant at lower currents.

The set of magnetogasdynamic numbers is shown in Fig. 12: magnetic Reynolds number, magnetic pressure number, Hartmann number and the magnetic parameter (square root of the ratio: magnetic force/inertial force). All numbers are averaged again through the orifice cross section. From the number's dependencies on arc current we can conclude that magnetic field is partially influenced by the arc motion (Magnetic Reynolds number is ~ 0.1); the magnetic pressure represents $\sim 0.05\text{--}0.08$ of the dynamic pressure; magnetic forces and viscous forces are comparable (Hartmann number ~ 1) and inertial forces are of the order of 10^3 with respect to magnetic forces.

At least two numbers reflecting the transfer of energy in the discharge are presented, namely, the Thring number Th (the ratio of convective heat transfer to radiation heat losses from the arc) and the Stefan number Sf (the ratio of radiation heat losses from the arc to conduction heat losses), see Fig. 13. It can be seen from the plots that the amount of power spent on convection (heating, ionization and acceleration of plasma) is comparable with radiation losses from the arc. Also, radiation losses increase with arc current and they are nearly 2 times higher than conduction losses. These results agree well with the conclusions made from approximate calculations based on experimental data.

Finally, we present some comparison of the present results with experiments made in IPP in the past [8] and with the other numerical simulation.

The current–voltage characteristics of the arc are presented in Fig. 14. One of the curves stands for the experimental measurements [8], two of the curves represent our numerical calculations: one of them is for the experimentally determined mass flow rates and the other one for the best-fit \dot{m} [25]. It is obvious that calculations with the fitted values of \dot{m} exhibit better agreement with experiments than the original calculations using the experimental values of \dot{m} . For comparison, current–voltage characteristics for an asymptotic arc region (1D model) are shown. This is the solution of the Elenbaas–Heller equation with the radiation term

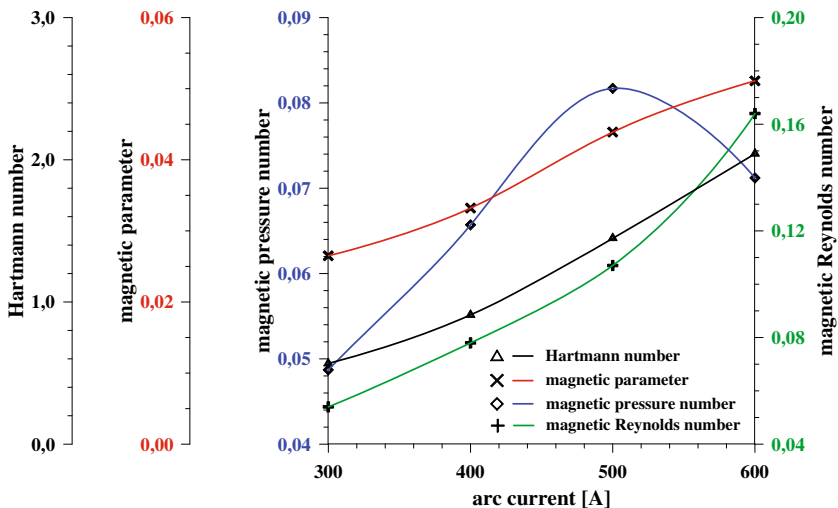


Fig. 12 Dimensionless magnetohydrodynamic numbers as a function of arc current. The dependences shown indicate the increasing importance of the magnetic field with current

Fig. 13 Dimensionless energy transfer numbers (Th—Thring number, Sf—Stefan number) as a function of arc current

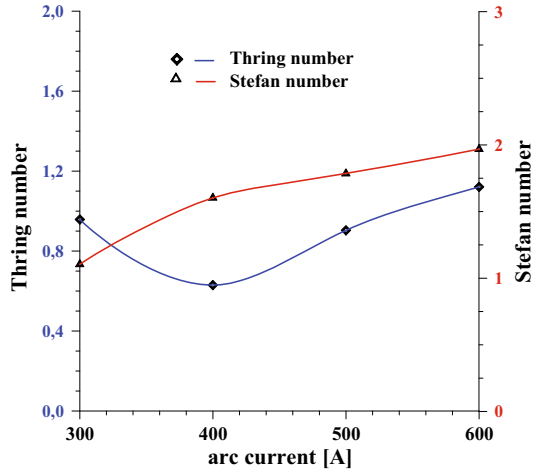
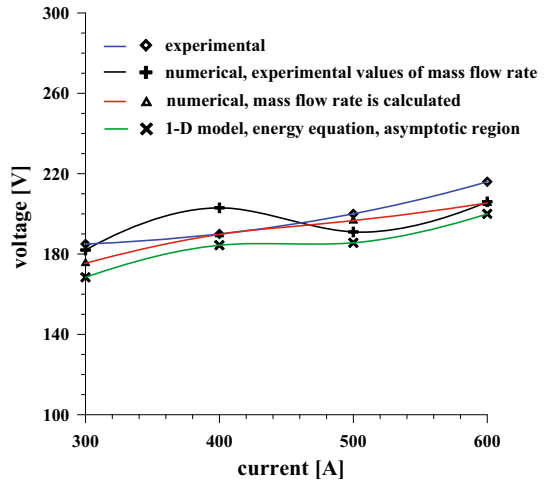


Fig. 14 Current–voltage characteristics. A solution of the Elenbaas–Heller equation with the radiation term (1-D model) is posted for a comparison



$$\sigma(T)E^2 + \frac{1}{r} \frac{d}{dr} \left(\lambda(T) \frac{dT}{dr} \right) - \Psi(T) = 0, \tag{9}$$

for the 65 mm long arc. The voltages obtained are not far from the experimental curve; thus to obtain an idea about the range of voltages in this kind of discharge, one can solve the Elenbaas–Heller equation instead of the complete 2D set of magnetohydrodynamic equations.

The next plot (Fig. 15) shows comparison of calculated and experimental radial velocity and temperature profiles. Negatively biased electric probes in ion collecting regime were used for determination of plasma flow velocity in experiments [8]. Temperature was evaluated from optical emission spectroscopy measurements [8, 10]. Calculations are taken at the nozzle exit, experiments 2 mm downstream of the nozzle exit. Comparison for velocity is very good for 300 and 400 A, with less than 500 m s⁻¹ velocity difference. For higher currents, with velocity difference of about 1–1.5 km s⁻¹, it is hard to make any

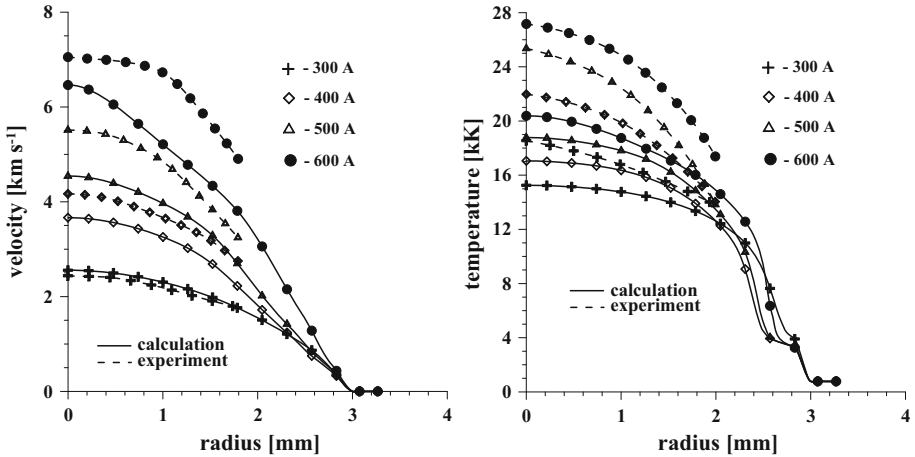


Fig. 15 Plots of calculated and experimental [8] radial velocity and temperature profiles with radiation calculated by the net emission model

conclusion in the sense “very good” or “good” agreement because error bars for this measurement are unavailable. All the calculated temperatures are lower than the experimental ones. For 300 A the temperature difference is about 1500 K which can be considered as a good agreement if we take some uncertainty of experimental measurements into consideration. For higher currents the temperature difference becomes much higher, exceeding the most probably temperature error bars, even though unknown. The main reason for the lower calculated temperatures at high currents consists in my opinion in the chosen radiation model (net emission coefficients [42]) which neglects reabsorption of radiation in the arc and the method of calculating of spectral line shapes. The more precise radiation model will be discussed in “[Reabsorption of Radiation in the Arc](#)” section.

Comparison of axial velocity and overpressure contours for 600 A with calculations made by Kotalík [35] is shown in Fig. 16. Despite both the codes use different numerical

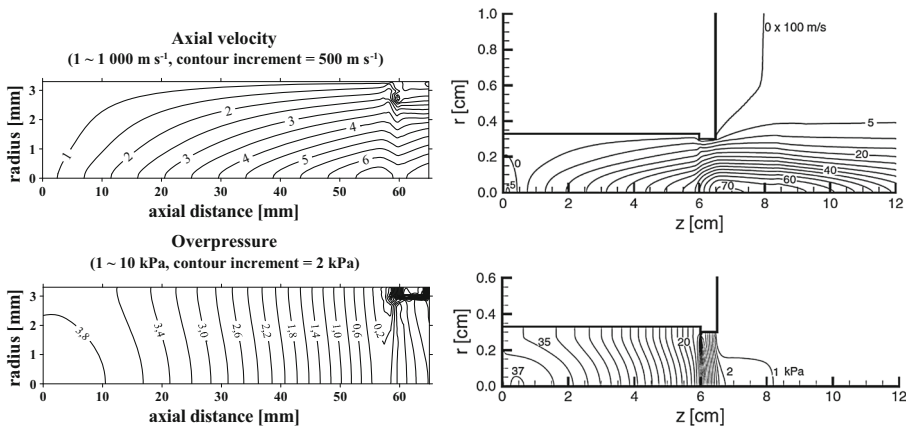


Fig. 16 Comparison between the present calculation (*left*) and those made by P. Kotalík [35] for 600 A. Despite some differences, velocity and overpressure contours reach similar values in both simulations

approach for solving the set of governing equations (my code—control volumes, Kotalík’s code—finite elements), and the boundary conditions are somehow different in the codes, contour profiles as well as the values of velocity and overpressure are very close.

Effect of the Tangential Velocity Component on the Arc Discharge Performance

In the water-vortex-stabilized plasma torch PAL 160, water is injected tangentially into the discharge chamber by several inlet apertures. Water is thus rotating in the chamber creating a water vortex. Going closer to the chamber axis, a water-steam phase transition takes place, followed by the so-called vapour region and, by the arc discharge zone at the axial region (electrically conducting plasma). It can be expected that, due to the viscosity of water, steam and plasma, part of the rotating momentum of a vortex is transferred to the arc plasma, i.e. the plasma discharge is rotating with nonzero tangential velocity. The distribution of this velocity component in the plasma as well as the impact on the overall arc performance were of interest of our research group.

The equation for the tangential velocity component w in the axisymmetric 2D case takes the form

$$\rho \frac{\partial w}{\partial t} + \rho v \frac{\partial w}{\partial r} + \rho u \frac{\partial w}{\partial x} = \frac{1}{r} \frac{\partial}{\partial r} \left(\eta r \frac{\partial w}{\partial r} \right) + \frac{\partial}{\partial x} \left(\eta \frac{\partial w}{\partial x} \right) - \frac{\rho v w}{r} - \frac{\eta w}{r^2} - \frac{w}{r} \frac{\partial \eta}{\partial r}, \quad (10)$$

where the term $\rho v w/r$ stands for Coriolis force. In the equation for the radial velocity component, the additional term $\rho w^2/r$ due to centrifugal forces appears; the axial momentum equation remains unchanged. Boundary conditions for (10) have to be specified before the start of numerical calculations. At the cathode $w = 0 \text{ m s}^{-1}$ (AB line, Fig. 4) because of no slip conditions. At the arc axis we prescribe a zero w -velocity. At the outlet CD we put $\partial w/\partial x = 0$ as the approximation (the same condition was applied for the v velocity). The only unknown boundary condition is the water-vapour surface AD, where a certain magnitude of the tangential component must be given.

At this stage I used the approximate approach by Maecker [3] where the tangential velocity is estimated from simplified analytical expressions. In this paper it is assumed that a water vortex at the vicinity of the arc region rotates with the same tangential velocity as the edge of the arc. The following analytical equation, originating from Bernoulli’s equation, for the tangential velocity component at the water-steam phase transition (with two possible real roots) can be derived:

$$p_L - p_i = \frac{\rho}{2} w_i^2 \left(2 \frac{w_a r_a}{w_i r_i} - 1 \right) \quad (11)$$

In this equation, p_L is the total pressure at the inlet apertures, p_i is the static pressure at the water-steam edge ($\sim 1 \text{ atm.}$), ρ is the water density, r_a is the radius of the chamber, r_i is the radius of the arc and vapour region, w_a is the inlet water velocity into the chamber and w_i is the calculated tangential velocity at the vapour region.

In the plasma torch, water is injected into the chamber usually under pressures of 0.39 MPa (0.6 MPa) with flow rates of 10 l min^{-1} (16 l min^{-1}). Under such conditions the inlet tangential velocity component is 10.5 m s^{-1} (16.8 m s^{-1}). The roots of the tangential velocity at the water-vapour interface are 7.3 m s^{-1} (79 m s^{-1}) for 0.39 MPa and 7.7 m s^{-1} (131 m s^{-1}) for 0.6 MPa. Since the water injected expands within the chamber volume and no additional forces influence its motion, we believe that the roots with lower

magnitudes of velocity will apply. Thus tangential velocities of the order of several meters per second are expected as realistic boundary condition for the AD line.

We carried out calculations for $w = 5, 10, 20, 30, 100, 150 \text{ m s}^{-1}$ as a boundary condition at AD and for currents 300, 400, 500 and 600 A. The results showed that the effect of the tangential velocity, in this range of velocities, on arc characteristics is small (the maximum difference in the outlet parameters is less than 2% regarding the case neglecting the tangential velocity). This is because centrifugal forces $\rho w^2/r$ appearing in the radial velocity equation are small compared to dominant terms in this equation. In order to demonstrate more precisely the magnitudes of different forces within the discharge, we present (Fig. 17) the following dimensionless numbers as functions of the arc current: Ekman number (square root of the ratio viscous force/Coriolis force), Rossby number (the ratio inertial force/Coriolis force), Taylor number (the ratio centrifugal force/viscous force). All numbers are mean values through the discharge cross section at the axial position 4.09 cm from the cathode. We can see that inertial forces are $\sim 10^3\text{--}10^4$ times higher than viscous and Coriolis forces. Viscous forces are several times higher than Coriolis forces, centrifugal forces are $\sim 10^3$ times lower than the viscous ones.

Some numerical results are presented in Figs. 18 and 19. Figure 18 depicts contours of the w velocity within the discharge for 300 and 600 A. A boundary condition $w = 10 \text{ m s}^{-1}$ at the AD line was employed. One can note immediately a qualitative difference between these two cases; the tangential velocity for lower currents decreases nearly monotonously to the arc axis while, for the higher current, the w velocity increases to peak values in front of the axis. Radial profiles of the tangential velocity (Fig. 19) reveal that the peak of the w velocity becomes more pronounced with increasing current. This behaviour is related to the temperature dependence of the dynamical viscosity. For higher currents, axial temperatures exceed 20,000 K and the dynamical viscosity rapidly decreases above these temperatures (the degree of ionization is more than 90%).

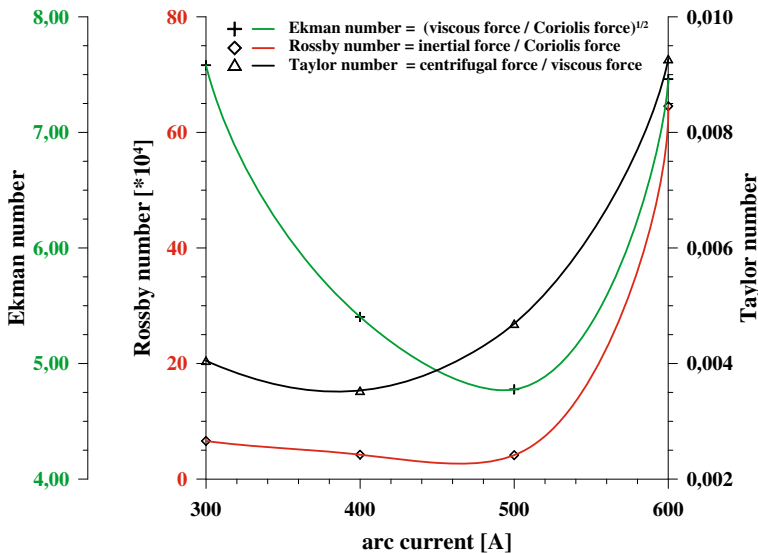


Fig. 17 Dimensionless mass transfer numbers (Ekman, Rossby, Taylor) as a function of arc current. All numbers are averaged through the discharge cross section

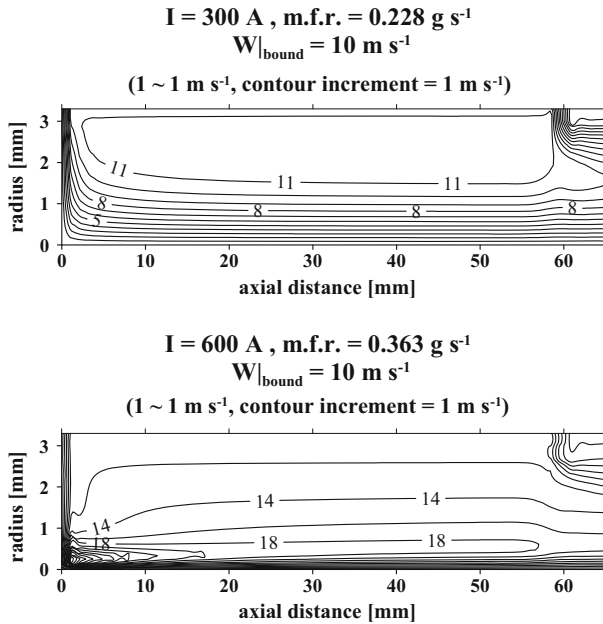
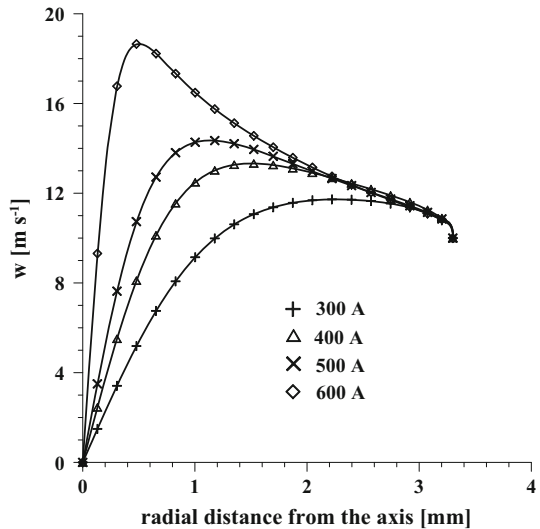


Fig. 18 Contours of the tangential velocity. For higher currents, the tangential velocity component increases near the axis due to the low dynamical viscosity of the plasma

Fig. 19 Radial profiles of the tangential velocity component w . The tangential velocity $w = 10 \text{ m s}^{-1}$ is prescribed at the boundary (3.3 mm), the axial distance from the cathode is 4.09 cm. The peaks of the w velocity become more pronounced for higher currents



A short analytical and simplified explanation for the velocity peaks can be done, for example, as follows: if the arc temperature increases, i.e. dynamical viscosity decreases, we get from (10), assuming the nearly asymptotic region inside the discharge ($\partial/\partial x \cong 0$), the equation

$$\frac{dw}{dr} = \frac{\frac{d\eta}{dr} + \rho v}{\frac{d\eta}{dr} - \rho v} \cdot \frac{w}{r} = \frac{1 + \frac{\rho v}{\frac{d\eta}{dr}}}{1 - \frac{\rho v}{\frac{d\eta}{dr}}} \cdot \frac{w}{r} \equiv f(r) \cdot \frac{w}{r}; \quad f(r) \equiv \frac{1 + \frac{\rho v}{\frac{d\eta}{dr}}}{1 - \frac{\rho v}{\frac{d\eta}{dr}}} \quad (12)$$

with the solution

$$w(r) = w(r_0) \cdot \exp\left(\int_{r_0}^r \frac{f(r)}{r} dr\right). \quad (13)$$

In the vicinity of r_0 , $f(r) \cong f(r_0)$ and the approximate solution of (13) reads

$$w(r) = w(r_0) \cdot \left(\frac{r}{r_0}\right)^{f(r_0)}. \quad (14)$$

Let us give the estimate for the 600 A discharge. For $r_0 = 0.47$ mm (the radial distance from the axis), $\rho v \sim -0.03$ kg m⁻² s⁻¹, $d\eta/dr \sim +0.02$ Pa s m⁻¹, $f(r_0) = -0.02$ which implies, if $r < r_0$, $w(r) > w(r_0)$. Thus the low dynamical viscosity in the axial region for higher currents is responsible for peaks in the tangential velocity component.

Experiments related to the rotation of the arc column were performed with water stabilized plasma torch described in [47]. The flow rate of stabilizing water through the torch was varied from 12 to 20 l min⁻¹ which results in variations of frequency of rotation of water vortex. Total mass flow rate of water plasma which is given by an evaporation rate from the inner wall of water vortex was 0.2–0.3 g s⁻¹ for arc power 100–200 kW. It was shown that the variations of flow rate have no effect on measured power balance of the torch and on measured mean values of voltage drop on different parts of the arc.

However, in the Fourier spectra of both voltage signals the same characteristic frequency in the range 250–450 Hz was found, which was dependent on water flow rate. The dependence of characteristic frequency on water flow rate and arc current was measured. In Fig. 20 the dependence of frequency on water flow rate is shown. The frequency is directly proportional to water flow rate and its value corresponds to estimated frequency of rotation in the stabilizing water vortex. Figure 21 presents dependence of characteristic frequency on arc current for two values of flow rate of water; 19.9 and 20.1 l min⁻¹. Small decrease of frequency was observed with increasing current.

We can conclude that the tornado effect under plasma conditions present in this kind of discharge has a negligible effect on arc characteristics, namely, on its power and force balances. Thus knowledge of exact value of the tangential velocity at the arc boundary or within the discharge region is not required.

Reabsorption of Radiation in the Arc

The water-vortex stabilized arc exhibits high radiation powers and radiation fluxes because it operates typically at currents 300–600 A, producing thus high-enthalpy oxygen-hydrogen plasma. Radiation in the numerical model must be treated very carefully to obtain relevant results. Simulations presented in preceding Sections employed the net emission coefficient which is quite popular among experts in thermal plasma community due to the simplicity of its use in the model. Application of the net emission coefficients to a prediction of energy balance gives good results for central arc temperatures, but it cannot predict accurate temperature profiles at low temperatures near the edge of the arc, because of the absorption of ultraviolet radiation emitted at the centre of the arc at high

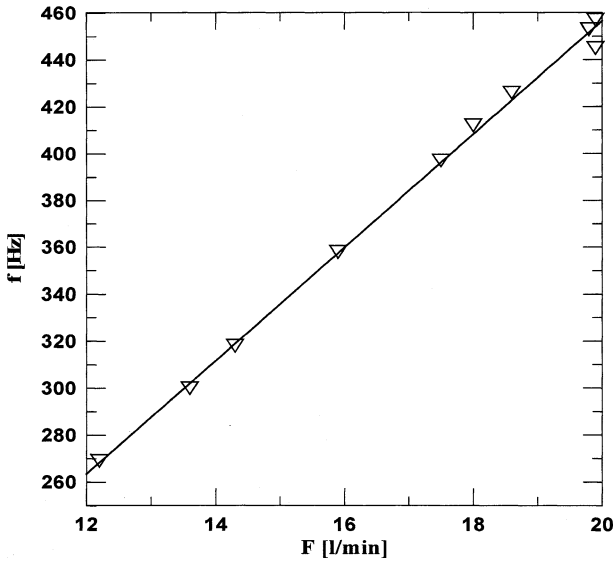


Fig. 20 The characteristic frequency of voltage fluctuations versus water flow rate (courtesy of Dr. Hrabovský)

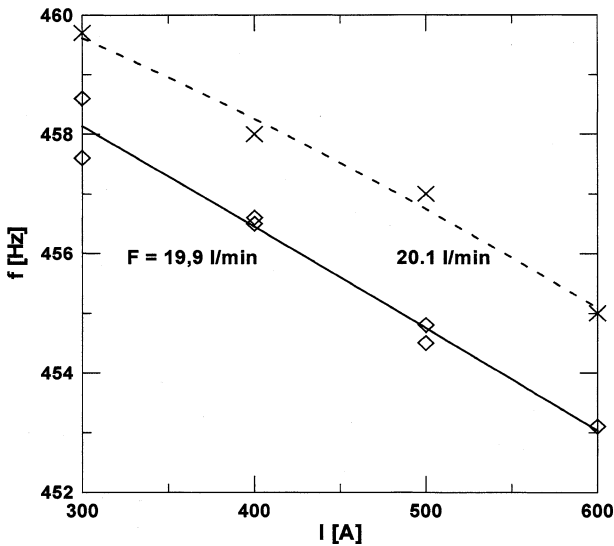


Fig. 21 The dependence of characteristic frequency of voltage fluctuations on arc current for two water flow rates (courtesy of Dr. Hrabovský)

temperatures (self absorption using this method can only be accounted for in a highly approximate way by using negative emission coefficients at low temperatures).

In this section the special method for calculation of radiation transfer was applied in our model, called the method of partial characteristics [48, 49]. This method was designed for radiation transfer in emitting and partially absorbing media, such in stellar atmospheres or

in electric arcs with plasmas in between optically thin and thick. The amount of self absorbed radiation in cold arc regions comes out from the calculation without any prior assumptions and constraints. In the following, when we mention ‘reabsorption’, ‘the reabsorption of radiation’ or ‘the impact of the reabsorption of radiation’, it refers to the reabsorption of radiation in the low temperature region in the partial characteristics method. A short description of the method is given here.

The principle of the method of partial characteristics is that integrals over radiation frequencies in equations for radiation quantities can be performed in advance to form functions Som and ΔSim , called partial characteristics [49, 50]. The partial characteristics include all time demanding integrations over frequencies. These functions are stored in data tables according to several parameters, such as plasma pressure, temperature and geometrical dimensions. The tables are then used for 3D computations with spatial integrations only.

The partial characteristics Som and ΔSim are defined as follows [50]:

$$Som(T_X, T_R, |R - X|) = \int_0^\infty B_\nu(X) \kappa_\nu(X) e^{-\int_X^R \kappa_\nu(\eta) d\eta} d\nu, \quad (15)$$

$$\Delta Sim(T_X, T_\xi, \xi - X) = \int_0^\infty [B_\nu(X) - B_\nu(\xi)] \kappa_\nu(X) \kappa_\nu(\xi) \exp\left(-\int_\xi^X \kappa_\nu(\eta) d\eta\right) d\nu \quad (16)$$

where B_ν is the Planck function, κ_ν is the absorption coefficient, T is the plasma temperature, and ξ, X, R are the radial coordinates. This method has been successfully used in some previous papers [51, 52] for prediction of radiation intensities, radiation fluxes and the divergence of radiation fluxes for various temperature profiles of SF₆ arc plasmas.

Note that if isothermal temperature profile is assumed, the function Som equals to the isothermal net emission coefficient introduced by Lowke [53] as

$$\varepsilon_N = \int_0^\infty B_\nu(T) \kappa_\nu(T, p) \exp[-\kappa_\nu(T, p)R] d\nu \quad (17)$$

where R represents the radius of plasma column. The ‘isothermal’ net emission coefficient, ε_N , corresponds to the fraction of the total power per unit volume and unit solid angle irradiated into a volume surrounding the axis of the arc and escaping from the arc column after crossing a thickness R of the isothermal plasma.

In the spectrum needed for the partial characteristics radiation model, continuous radiation due to photorecombination and ‘bremsstrahlung’ processes has been included as well as discrete radiation consisting of thousands of spectral lines. Broadening mechanisms of atomic and ionic spectral lines due to Doppler, resonance and Stark effects have been considered. The numbers of oxygen lines included in the calculation are O (93 lines), O⁺ (296 lines), O₂⁺ (190 lines). In addition, molecular bands of O₂ (Schuman–Runge system), H₂ (Lyman and Verner systems), OH (transition A²Σ⁺ → X²Π₁) and H₂O (several transitions) have been also implemented [54]. Absorption coefficient as a function of wavelength has been calculated from infrared to far ultraviolet regions and the tables of partial characteristics for 1–35 kK.

We also assumed the linear dependence of the density ρ and the radiation losses \dot{R} from the arc on pressure:

$$\rho(p, T) = \frac{P}{p_{atm.}} \rho(p_{atm.}, T), \quad \dot{R}(p, T) = \frac{P}{p_{atm.}} \dot{R}(p_{atm.}, T), \quad (18)$$

The linear dependence of density on pressure follows from the equation of state for ideal gas; the linear dependence of the radiation losses is an approximation of the fact that radiation losses increase with operating pressure. Similar approach for the net emission coefficient has been applied by other authors [55].

Calculations have been carried out for currents 150–600 A with the steam mass flow rates between 0.0843 g s⁻¹ (150 A) and 0.363 g s⁻¹ (600 A).

Figure 22 demonstrates the input power and power losses from the arc discharge as a function of current. The term input power means the product of current and the potential drop in the discharge chamber. The power losses from the arc stand for the radial conduction power and radiation power leaving the discharge which are considered as the two principal processes responsible for power losses. The input power is approximately six times higher for the 600 A arc (~110 kW) than for 150 A. The absolute value of the power losses increase with current but the ratio of the power losses to the input power decrease approximately from 60 to 30%. The amount of reabsorbed radiation in the partial characteristics model divided by the total divergence of radiation flux is between 17 and 28%.

Figures 23 and 24 show contours of the divergence of radiation flux (W m⁻³) and the radiation flux (W m⁻²) for 300 and 600 A. The axial position 0 mm (65 mm) corresponds to the cathode (outlet). Orientation of the domain is the same as in Fig. 4. The maximum radiation power occurs in the arc centre, the reabsorbing boundary with the zero value is located at the radial positions around 2.5 mm for 300 A and 2.7 mm for 600 A. The maximum radiation flux is shifted at 600 A towards arc fringes. The pressure dependence is evident in all contours—overpressure increases in the discharge towards the cathode.

The corresponding temperature and velocity contours are given in Figs. 25 and 26. The maximum axial velocity and temperature for 600 A are 8500 m s⁻¹ and 26,300 K. It was shown that reabsorption of radiation results generally in flatter radial temperature profiles within the arc and higher temperatures at the arc boundary. The current-carrying arc core becomes wider and a lower potential drop is able to maintain the discharge.

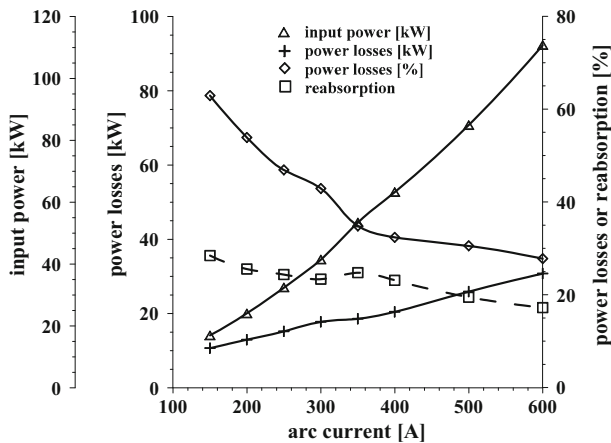


Fig. 22 Input power (kW), power losses by conduction and radiation (kW, %), and the amount of reabsorbed radiation vs arc current (%)

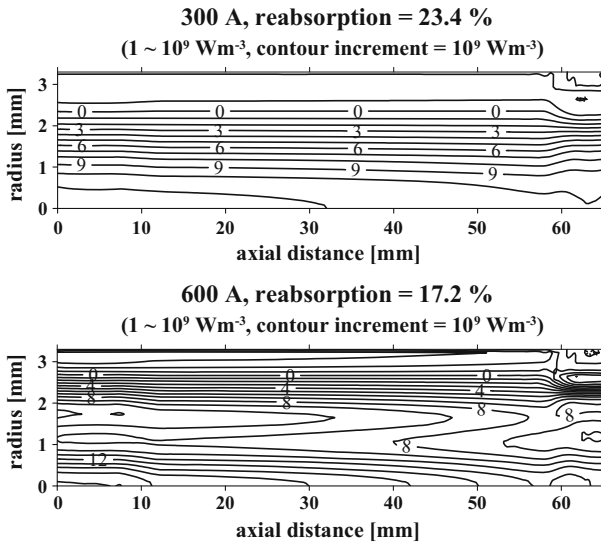


Fig. 23 Contours of the divergence of radiation flux (W m^{-3}) for the partial characteristics model for 300 and 600 A. 10^9 W m^{-3} corresponds to 1 in the plot

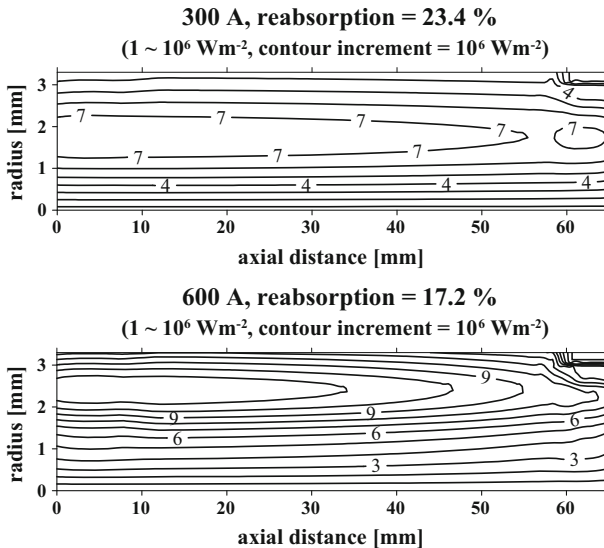


Fig. 24 Contours of the radiation flux (W m^{-2}) for the partial characteristics model for 300 and 600 A. 10^6 W m^{-2} corresponds to 1 in the plot

Finally, comparison between experimental and calculated radial velocity and temperature profiles for the partial characteristics method employed in the calculations is shown in Fig. 27. Again, position of numerical curves is exactly at the nozzle exit, experimental curves are taken 2 mm downstream of the nozzle exit. Calculated temperatures are now much higher than in Fig. 15 (with the net emission radiation method employed) and the

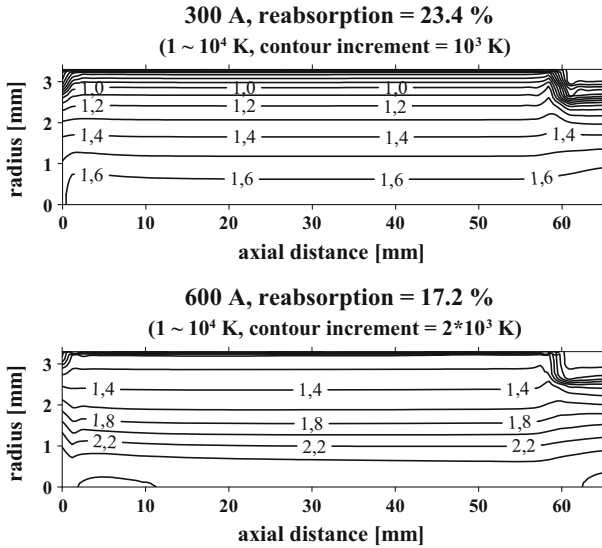


Fig. 25 Temperature contours for 300 and 600 A. 10^4 K corresponds to 1 in the plot

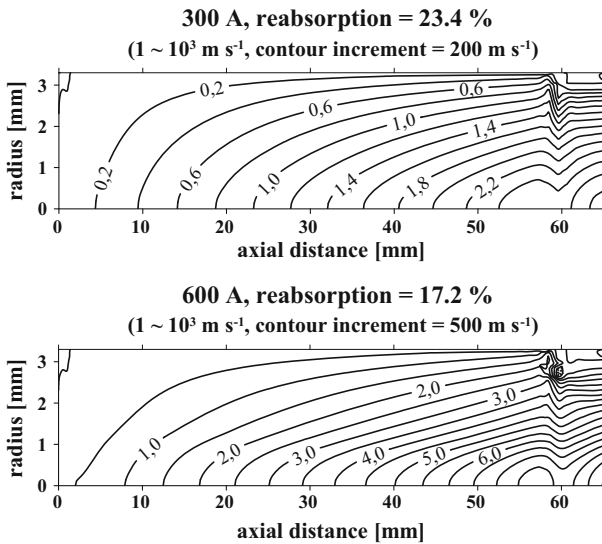


Fig. 26 Velocity contours for 300 and 600 A. 1000 m s^{-1} corresponds to 1 in the plot

profiles show good agreement for all currents. Velocity profiles at the radial distances 1–2 mm are very close to each other, while at the axial region the calculated profiles are somewhat higher (500–600 A). This can be caused, besides other things, by the simplified assumption of the constant Mach number over the nozzle radius in the experimental evaluation of the outlet velocity, decreasing thus real velocity values.

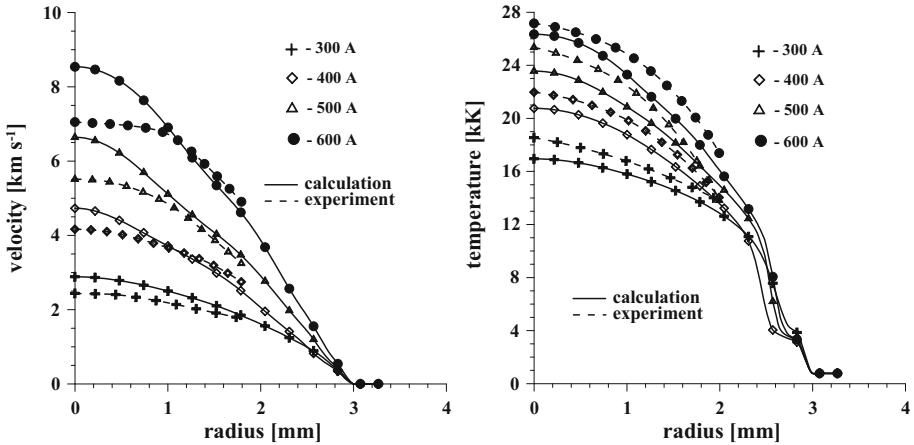


Fig. 27 Plots of calculated and experimental [8] radial velocity and temperature profiles with radiation calculated by the partial characteristics model

Non-equilibrium Effects

In a PhD thesis [10] it was shown that a significant underpopulation of atomic and ionic excited states in the water-vortex stabilized arc discharge can be expected, having a strong impact on energy balance in the plasma jet. Deviations from local thermodynamic equilibrium (LTE) in the water plasma torch can occur in the first place as a result of strong temperature and density gradients that give rise to transport phenomena as a rapid diffusion of particles and radiation escape—the rate of which can exceed the rate of a dominant collisional process. Furthermore, in high-speed plasma flows (such as in water-vortex stabilized arc regimes), strong deviations from chemical equilibrium are likely because of the finite rates and thus finite times of reactions involved in the plasma. To make an exact analysis of non-equilibrium effects in the water plasma, the effects of the departures from the both kinetic and chemical equilibrium should be discussed. Chemical non-equilibrium effects can be generally rigorously studied by two-temperature numerical model, including the set of diffusion equations for plasma species with the net rate of production of species determined by the proper plasma kinetics, two-temperature Saha equations, and collision cross sections and plasma properties depending on a local temperature (either electron or heavy species), pressure and particle number density. Since the present numerical model of the water arc discharge is one-fluid and one-temperature, assuming the LTE composition of plasma species, I can consider here only the effects of kinetic non-equilibrium.

In the following we estimate the validity of LTE conditions within the arc column by means of the criteria for the kinetic equilibrium and spatial variations of temperature [56]

$$\frac{T_e - T}{T_e} = \frac{\pi m_h}{24 m_e} \left(\frac{e \lambda_e E}{k T_e} \right)^2, \quad \lambda_e \frac{\nabla T}{T} < < 1, \tag{19}$$

where $T_e(T)$ denotes the electron (heavy species) temperature, $m_e(m_h)$ the electron (heavy species) mass, λ_e the mean free path of electrons, E the electric field strength, k the

Boltzmann constant. For simplification we included in the calculation of mean free path only collision cross sections electrons-ions, i.e. we suppose fully-ionized approach enabling to calculate the cross sections using the analytical Spitzer–Harm formulae [57]. We thus consider in this analysis only the arc regions with temperatures higher than 9000 K, i.e. with the degree of ionization higher than 2%.

Figure 28 (left) presents radial profiles of deviations from the kinetic equilibrium for several values of current. The axial position from the cathode is 4.08 cm. Within the arc radius 2 mm, deviations below 3% occur for all currents. For the arc radii higher than 2 mm, deviations start to rise steeply and the fulfilment of the kinetic equilibrium condition is better for higher currents. At the edge of the plasma column but with temperatures still above 9000 K, deviations range between 34% (for 300 A) and 52% (for 600 A). However, it can be expected that the maximum values of the relative deviation at the arc edge could be somehow lower in reality; likely because (Eq. 19) was calculated for a fully-ionized plasma, neglecting inelastic collisions due to electron-neutral and ion-neutral collisions, which start to be important at low degrees of ionization, causing the decrease of mean free path of electrons. The real deviation from LTE at the plasma edge (~ 9000 K) is expected to be somewhat lower than the values plotted in Fig. 28 (left).

Figure 28 (right) shows relative deviations from the kinetic equilibrium as a function of arc current. Radial positions 2 and 2.7 mm from the axis are taken again at a distance of 4.08 cm downstream of the cathode. High increase of kinetic nonequilibrium is obvious at the radial distance of 2.7 mm compared to the values of deviations at 2 mm. It can be also seen that fulfillment of LTE conditions is better for higher currents.

Deviations due to the spatial variation of temperature (Fig. 29) are below 0.1% in the arc core and 0.1–1% in arc fringes, and they are about one order lower than the departures estimated from the ratio of energy gained by the electric field and the thermal energy

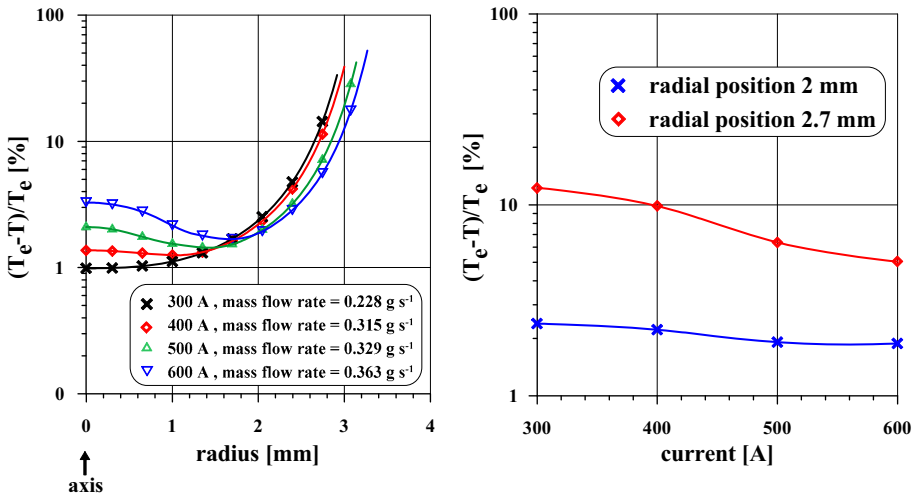
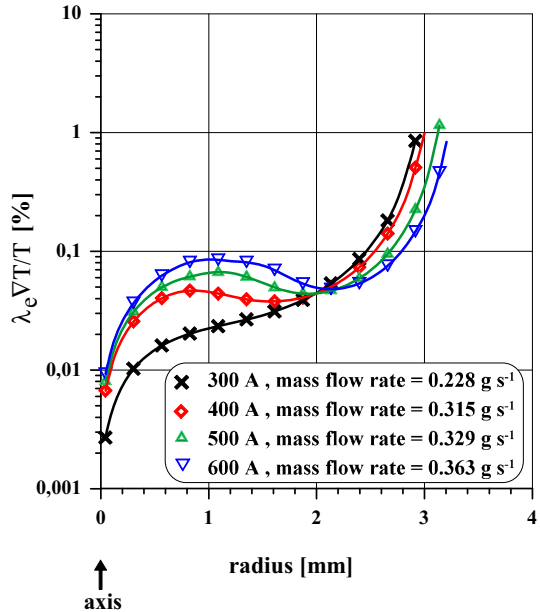


Fig. 28 Relative deviations from the kinetic equilibrium (%) as a function of radial position and current. Radial profiles (left) as well as the radial positions (right) are taken at a distance of 4.08 cm downstream of the cathode

Fig. 29 Relative deviations from the spatial temperature gradients (%) as a function of radial position and current. λ_e depicts the mean free path of electrons. Axial position from the cathode is 4.08 cm



(Fig. 28). Temperature gradients inside the discharge chamber thus does not seem to be a principal mechanism of substantial deviations from LTE.

Conclusions

This review paper summarizes the most important numerical results of the electric arc stabilized by a water vortex obtained during the years 1997–2006. The two-and-half axisymmetric numerical model of the arc stabilized by a water vortex, based on the control volume method, explains the arc properties and basic physical processes in the discharge chamber. The steady state computer results of thermal, fluid dynamic and electrical characteristics of such arc are shown mostly for the currents 300–600 A with steam flow rate of about 0.3 g s^{-1} .

Using a comparison between the present simulation and experiments, the production of plasma material, i.e. evaporation of water (generation of steam) was predicted. The numerical values of evaporation mass flow rates are higher by about 20% from the values predicted from experiments— 0.228 g s^{-1} (300 A); 0.315 g s^{-1} (400 A); 0.329 g s^{-1} (500 A) and 0.363 g s^{-1} (600 A). These mass flow rates were employed in our simulations.

Our calculations showed that there is a nearly fully-developed thermal region in the discharge channel with a length of ~ 4 cm. Temperature gradients in the vapour region ($T < 7000 \text{ K}$) are steeper for higher currents. Plasma velocity increases towards the nozzle due to continuous evaporation of steam from water column. For 600 A the maximum velocity at the nozzle axis is 6500 m s^{-1} . Since the electric equipotential lines are nearly perpendicular to the arc axis, the arc current flows in the axial direction.

In the arc energy balance, the most significant processes determining properties of the arc are the mutual balance of the Joule heat with radiation and radial conduction losses. The main driving forces for the velocity are gradients of static pressure and the Lorentz

force. Non-dimensional analysis based on similarity fluid-dynamic, magnetohydrodynamic and thermal numbers showed that with increasing current the plasma becomes more compressible, the viscous stresses decrease and the role of thermal diffusion and convection increases. Further, magnetic field is only partially influenced by the arc motion (Magnetic Reynolds number is ~ 0.1); the magnetic pressure represents $\sim 10^{-2}$ of the dynamic pressure; magnetic forces and viscous forces are comparable and the inertial forces are of the order of 10^3 with respect to magnetic forces. Inertial forces are of the order of 10^3 to the magnetic, viscous, centrifugal and Coriolis forces within the arc discharge.

The attention has been paid to the vortex motion of the arc. It was numerically confirmed that rotation of plasma column due to tangential velocity components has a negligible effect on the overall arc performance. For higher currents, the tangential velocity component increases near the axis due to low dynamical plasma viscosity. In experiment, the rotation of water induces fluctuations in the arc and in plasma jet with characteristic frequency which is related to the frequency of rotation of water which are probably caused by small asymmetry of the vortex in the arc chamber.

Applying the partial characteristics model for radiation, self-absorption (or reabsorption) within the arc was calculated. The reabsorbing boundary with the zero value of the radiation losses is located around 2.5 mm radially from the discharge axis at 300 A and 2.7 mm at 600 A. The amount of reabsorbed radiation in the partial characteristics model divided by the total divergence of radiation flux is between 17 and 28%. The absolute value of the power losses, calculated using this radiation model, increase with current but the ratio of the power losses to the input power decrease from 60 to 30%.

In the arc core, at the radial positions less than 2 mm, the maximum deviation from the kinetic LTE is below 3%. For higher currents the fulfilment of the kinetic equilibrium condition is better. Deviations due to the spatial temperature gradients in the whole plasma discharge are less than 1%, thus the gradients do not seem to be a driving force for substantial nonequilibrium effects in the discharge.

Where possible, comparisons between simulations and experiments show mostly good agreement (the current–voltage characteristics, radial velocity and temperature profiles for the partial characteristics radiation model). Comparison between the present simulation and the chosen plots in [35] exhibit also good agreement.

In conclusion it can be said that the present model can be used to predict the basic properties of the steam plasma torch with the water-vortex stabilization of the electric arc.

Acknowledgements The author would like to thank Assoc. Prof. M. Hrabovský for many helpful discussions throughout the years in IPP. This work has been supported by the Grant Agency of the Czech Republic under the grant number GA15-19444S. Our appreciation goes also to the computational resources, provided by the CESNET LM2015042 and the CERIT Scientific Cloud LM2015085, provided under the programme “Projects of Large Research, Development, and Innovations Infrastructures”.

References

1. Gerdien H, Lotz A (1922) *Wiss Veröffentlichungen Siemenswerk* 2:489
2. Gerdien H, Lotz A (1923) *Z Tech Phys* 4:157
3. Maecker H (1951) *Z Phys* 129:108–122
4. Burnhorn F, Maecker H (1951) *Z Phys* 129:369–376
5. Larentz RW (1951) *Z Phys* 129:343–364
6. Weiss R (1954) *Z Phys* 138:170–182

7. Burnhorn F, Maecker H, Peters T (1951) *Z Phys* 131:28–40
8. Hrabovský M, Konrád M, Kopecký V, Sember V (1997) *IEEE Trans Plasma Sci* 25:833–839
9. Hrabovský M, Kopecký V, Sember V (1994) Heat and mass transfer under plasma conditions. Begell House, New York, pp 91–98
10. Sember V (1998) CSc. PhD thesis, Academy of Sciences of the Czech Republic, Praha
11. Hrabovský M, Konrád M, Kopecký V (1994) Heat and mass transfer under plasma conditions. Begell House, New York, pp 61–67
12. Chráška P, Hrabovský M (1992) In: Berndt CC (ed) *International Thermal Spray Conference*, Orlando, FL, May 28–June 5, ASM International, Materials Park, OH, USA, pp 81–85
13. Gross B, Grycz B, Miklossy K (1968) *Plasma technology*. Iliffe, London
14. Chráška T, Neufuss C, Dubský J, Ctibor P, Klementová M (2008) *J Therm Spray Technol* 17:872–877
15. Chráška T, Hostomský J, Klementová M, Dubský J (2009) *J Eur Ceram Soc* 29:3159–3165
16. Ctibor P, Ageorges H, Sedláček J, Čtvrtlík R (2010) *Ceram Int* 36:2155–2162
17. Štengl V, Ageorges H, Ctibor P, Murařa N (2009) *Photochem Photobiol Sci* 8:733–738
18. Van Oost G, Hrabovský M, Kopecký V, Konrád M, Hlína M, Kavka T, Chumak O, Beeckman E, Verstraeten J (2006) *Vacuum* 80:1132–1137
19. Van Oost G, Hrabovský M, Kopecký V, Konrád M, Hlína M, Kavka T (2009) *Vacuum* 83:209–212
20. Van Oost G, Hrabovsky M, Khvedchyn I, Sauchyn V, Shvarkov D (2013) *Vacuum* 88:165–168
21. Lafon Ch, Girold Ch, Lemort F, Baronnet JM (2003) In: *The 1st European Hydrogen Energy Conference, EHEC 2003, Grenoble, 2–5 September 2003*, CP1/135
22. Jeništa J (1999) *J Phys D Appl Phys* 32:2763–2776
23. Jeništa J (1999) *J Phys D Appl Phys* 32:2777–2784
24. Gonzalez JJ, Jeništa J (1999) In: Hrabovský M, Konrád M, Kopecký V (eds) *Proceedings of 14th international symposium plasma chemistry, LOC of the 14th ISPC*, pp 355–360
25. Jeništa J (2003) *J Phys D Appl Phys* 36:2995–3006
26. Jeništa J (2003) *J High Temp Mater Process* 7:11–16
27. Jeništa J (2000) *Czech J Phys* 50(Suppl. S3):281–284
28. Jeništa J, Bartlová M, Aubrecht V (2004) *J High Temp Mater Process* 8:195–206
29. Jeništa J, Bartlová M, Aubrecht V (2006) *Czech J Phys* 56(Suppl. B):B1224–B1230
30. Jeništa J, Bartlová M, Aubrecht V (2007) In: *Complex Systems, AIP Conference Proceedings* 982:554–560
31. Matas R (2001) In: *Fluent 2001—7th User’s Conference, Třeří, Sept. 19–1, 2001*, pp 67–70 (in Czech)
32. Kotalík P (1998) In: *Badalec J, Stockel J, Šunka P, Tendler M (eds) Proceedings of 25th international congress on plasma physics, European Physical Society*, pp 2710–2713
33. Kotalík P (1999) PhD thesis, No. 4510, Central library of MFF UK, Centre for scientific informations, Praha
34. Kotalík P (1999) In: Hrabovský M, Konrád M, Kopecký V (eds) *14th International symposium on plasma chemistry (ISPC 14), LOC of the 14th ISPC*, pp 397–402
35. Kotalík P (2006) *J Phys D Appl Phys* 39:2522–2533
36. Kotalík P (1993) *Czech J Phys B* 43:1165–1171
37. Kotalík P (1996) *Czech J Phys B* 46:793–801
38. Chau SW, Lub SY, Wang PJ (2011) *Comput Phys Commun* 182:152–154
39. Chau SW, Hsu KL (2011) *Comput Fluids* 45:109–115
40. Chau SW, Tai CM, Chen SH (2014) *IEEE Trans Plasma Sci* 42:3797–3808
41. Křenek P, Hrabovský M (1993) In: *Harry J (ed) Proceedings of 11th international symposium on plasma chemistry (ISPC-11), IOC of the 11th ISPC*, pp 315–320
42. Gleizes A, Gonzalez JJ, Riad H (1995) In: *Heberlein JV, Ernie DW, Roberts JT (eds) Proceedings of 12th international symposium on plasma chemistry (ISPC 12), IOC of the 12th ISPC*, pp 1731–1736
43. Sember V (1994) Heat and mass transfer under plasma conditions. Begell House, New York, pp 143–149
44. Patanakar SV (1980) *Numerical heat transfer and fluid flow*. McGraw-Hill, New York
45. Hrabovský M, Konrád M, Kopecký V, Sember V (1995) In: *Heberlein JV, Ernie DW, Roberts JT (eds) Proceedings of 12th international symposium on plasma chemistry (ISPC 12), IOC of the 12th ISPC*, pp 1627–1632
46. Jeništa J (2000) *Czech J Phys* 50(Suppl. S3):281–284
47. Jeništa J, Kopecký V, Hrabovský M (1999) In: *Fauchais P et al (eds) Heat and Mass Transfer under Plasma Conditions—Annals of the New York Academy of Sciences* 891:64–71
48. Soloukhin RI (1980) *Radiative heat transfer in high-temperature gases*. Hemisphere, London
49. Sevast’yanenko VG (1979) *J. Eng Physics* 36:138–148

50. Aubrecht V, Bartlová M, Urban F, Valenta J (2004) In: Bordage MC, Gleizes A, Gonzalez JJ (eds) Proceedings of 15th international conference gas discharges and their applications (GD 2004), LOC of GD 2004, pp 141–144
51. Aubrecht V, Lowke JJ (1994) *J Phys D Appl Phys* 27:2066–2073
52. Aubrecht V, Bartlová M (1997) *IEEE Trans Plasma Sci* 25:815–823
53. Liebermann RW, Lowke JJ (1976) *J Quant Spectrosc Radiat Transf* 16:253–264
54. Bartlová M, Aubrecht V (2006) *Czech J Phys* 56(Suppl. B):B632–B637
55. Freton P, Gonzalez JJ, Gleizes A, Peyret FC, Caillibotte G, Delzenne M (2002) *J Phys D Appl Phys* 35:115–131
56. Boulos MI, Fauchais P, Pfender E (1994) *Thermal plasmas*. Plenum Press, New York
57. Mitchner M, Kruger CH Jr (1973) *Partially ionized gases*. Wiley, New York